

Omnipose: a high-precision morphology-independent solution for bacterial cell segmentation

Kevin J. Cutler¹, Carsen Stringer², Paul A. Wiggins^{1,3,*} and Joseph D. Mougous^{4,5,*}

¹Department of Physics, University of Washington, Seattle, WA 98195, USA

²HHMI Janelia Research Campus, Ashburn, VA, USA

³Department of Bioengineering, University of Washington, Seattle, WA 98195, USA

⁴Department of Microbiology, University of Washington, Seattle, WA 98109, USA

⁵Howard Hughes Medical Institute, University of Washington, Seattle, WA 98195, USA

* To whom correspondence should be addressed:

Email – pwiggins@uw.edu, mougous@uw.edu

1 **Abstract**

2 Advances in microscopy hold great promise for allowing quantitative and precise
3 readouts of morphological and molecular phenomena at the single cell level in bacteria.
4 However, the potential of this approach is ultimately limited by the availability of
5 methods to perform unbiased cell segmentation, defined as the ability to faithfully
6 identify cells independent of their morphology or optical characteristics. In this study, we
7 present a new algorithm, Omnipose, which accurately segments samples that present
8 significant challenges to current algorithms, including mixed bacterial cultures,
9 antibiotic-treated cells, and cells of extended or branched morphology. We show that
10 Omnipose achieves generality and performance beyond leading algorithms and its
11 predecessor, Cellpose, by virtue of unique neural network outputs such as the gradient of
12 the distance field. Finally, we demonstrate the utility of Omnipose in the characterization
13 of extreme morphological phenotypes that arise during interbacterial antagonism and on
14 the segmentation of non-bacterial objects. Our results distinguish Omnipose as a uniquely
15 powerful tool for answering diverse questions in bacterial cell biology.

16 **Introduction**

17 Although light microscopy is a valuable tool for characterizing cellular and sub-
18 cellular structures and dynamics, quantitative analysis of microscopic data remains a
19 persistent challenge¹. This is especially pertinent to the study of bacteria, many of which
20 have dimensions in the range of optical wavelengths. Thus, their cell body is composed
21 of a small number of pixels (*e.g.*, $\sim 100\text{-}300 \text{ px}^2$ for *E. coli* at 100x magnification). At this
22 scale, accurate subcellular localization requires defining the cell boundary with single-
23 pixel precision. The process of defining cell boundaries within micrographs is termed cell
24 segmentation and this is a critical first step in current image analysis pipelines^{2,3}.

25 In addition to their small size, bacteria adopt a wide range of morphologies.
26 Although many commonly studied bacteria are well-approximated by idealized rods or
27 spheres, there is growing interest in bacteria with more elaborate shapes⁴. Some examples
28 include Streptomycetales, which form long filamentous and branched hyphal structures⁵,
29 and Caulobacterales, which generate extended appendages distinct from their cytoplasm⁶.
30 Furthermore, microfluidic devices are allowing researchers to capture the responses of
31 bacteria to assorted treatments such as antibiotics, which often result in highly irregular
32 morphologies⁷. Whether native or induced, atypical cell morphologies present a distinct
33 problem at the cell segmentation phase of image analysis^{8,9}. This is compounded when
34 such cells are present with those adopting other morphologies, as is the case in many
35 natural samples of interest¹⁰. To date, there are no solutions for segmenting bacterial cells
36 of assorted shape and size in a generalizable manner¹.

37 Cell segmentation is a complex problem that extends beyond microbiological
38 research, thus many solutions are currently available in image analysis programs^{8,9,11-27}.

39 Most of these solutions use traditional image processing techniques such as the
40 application of an intensity threshold to segment isolated cells; however, this approach
41 does not perform well for cells in close contact and it requires extensive parameter-tuning
42 in order to optimize for a given cell type. SuperSegger was developed to address these
43 issues specifically in bacterial phase contrast images¹³. This program utilizes both
44 traditional image filtering techniques and a shallow neural network to correct for errors
45 that thresholding and watershed segmentation tend to produce.

46 Deep neural networks (DNNs) are now widely recognized as superior tools for
47 cell segmentation²⁸. Unlike traditional image processing, machine-learning approaches
48 such as DNNs require training on a ground-truth dataset of cells and corresponding
49 labels. Trained DNNs are thus limited in applicability to images that are representative of
50 those in the training dataset. Early DNN approaches were based on the Mask R-CNN
51 architecture²⁴, whereas more recent algorithms such as StarDist, Cellpose, and MiSiC are
52 based on the U-Net architecture^{12,15,26}. Pachitariu and colleagues showed that Cellpose
53 outperforms Mask R-CNN and StarDist on a variety of cell types and cell-like objects,
54 distinguishing it as a general solution for cell segmentation¹². Notably, the representation
55 of bacteria in their study was limited. MiSiC was developed as a general DNN-based
56 solution for bacterial segmentation; however, the authors of MiSiC did not provide
57 comparisons to other DNN algorithms¹⁵. Here, we evaluated the performance of state-of-
58 the-art cell segmentation algorithms on a diverse collection of bacterial cells. Our
59 findings motivated the design of a new algorithm, Omnipose, that significantly
60 outperforms all previous cell segmentation algorithms across a wide range of bacterial
61 cell sizes, morphologies, and optical characteristics. We have made Omnipose and all

62 associated data immediately available to researchers, and we anticipate that our model –
63 without retraining – can be applied to diverse bacteriological systems. Furthermore,
64 following the incorporation of additional ground truth data, Omnipose could serve as a
65 platform for segmenting various eukaryotic cells and extended, anisotropic objects more
66 broadly.

67

68 **Results**

69 **Evaluation of bacterial cell segmentation algorithms**

70 Numerous image segmentation algorithms have been developed, and the
71 performance of many of these on bacterial cells is documented¹. These broadly fall into
72 three categories: *(i)* traditional image processing approaches (*e.g.*, thresholding,
73 watershed), *(ii)* traditional/machine learning hybrid approaches, and *(iii)* deep neural
74 network (DNN) approaches. Given the goal of developing software with the capacity to
75 recognize bacteria universally, we sought to identify strongly performing algorithms for
76 further development. An unbiased, quantitative comparison of cell segmentation
77 algorithms on bacterial cells has not been performed; thus, we selected one or more
78 representatives from each category for our analysis: Morphometrics²³ *(i)*, SuperSegger¹³
79 *(ii)*, Mask R-CNN²⁷, StarDist²⁶, MiSiC¹⁵, and Cellpose¹² *(iii)*. For a detailed review of
80 these choices, see Methods.

81 For training and benchmarking these algorithms, we acquired micrographs of
82 assorted bacterial species representing diverse morphologies and optical characteristics.
83 Many studies of bacteria involve mutations or treatments that cause extreme
84 morphologies. To capture this additional diversity, we included wild-type and mutant

85 bacteria grown in the presence of two beta-lactam antibiotics, cephalexin and aztreonam,
86 and A22, which targets MreB²⁹. Finally, based on our interest in microbial communities,
87 we acquired images of mixtures of bacteria which display distinct morphologies and
88 optical characteristics. In total, we collected 4833 images constituting approximately
89 700,900 individual cells deriving from 14 species (Extended Data Table 1). Next, we
90 developed a streamlined approach for manual cell annotation and applied it to these
91 images (see Methods), yielding 46,000 representative annotated cells that serve as our
92 ground-truth dataset. We arbitrarily split this data into a 27,000-cell training set and a
93 19,000-cell benchmarking set. Relevant cellular metrics did not differ substantially
94 between the groups, confirming that the benchmarking set faithfully represents the
95 training set (Extended Data Fig. 1).

96 To facilitate direct comparison of the algorithms, we first optimized their
97 performance against our data. For the DNN approaches, each algorithm was trained on
98 our dataset using developer-recommended parameters. Morphometrics and SuperSegger
99 cannot be automatically optimized using ground-truth data; therefore, we manually
100 identified settings that optimized the performance of these algorithms against our dataset
101 (see Methods). As a quantitative measure for algorithm performance, we compared their
102 average Jaccard Index (JI) as a function of intersection over union (IoU) threshold – a
103 well-documented approach for evaluating image segmentation (Fig. 1a)^{30,31}. IoU values
104 lie between zero and one, with values greater than 0.8 marking the point at which masks
105 become indistinguishable from ground truth by the expert human eye (Extended Data
106 Fig. 2)³⁰. This analysis showed that DNN-based approaches significantly outperform
107 other algorithms. However, within the DNN group, substantial differences in

108 performance were observed; Cellpose and StarDist outperform Mask R-CNN and MiSiC
109 at high IoU thresholds. The performance of all algorithms varied greatly across the
110 images in our ground-truth dataset, with much of this variability delineated by cell type
111 and morphology categories (Fig. 1b-g). Whereas all other algorithms exhibited visible
112 segmentation errors in two of the three cell categories we defined, errors by Cellpose –
113 the best overall performing algorithm at high IoU thresholds – were only apparent in
114 elongated cells (Fig. 1h-j).

115

116 **Motivation for a new DNN-based segmentation algorithm**

117 Our comparison revealed that Cellpose offers superior performance relative to the
118 other segmentation algorithms we analyzed, and for this reason, we selected this
119 algorithm for further development. Notably, even at the high performance levels of
120 Cellpose, only 83% of predictions on our benchmarking dataset are above 0.8 IoU. This
121 limits the feasibility of highly quantitative studies such as those involving subcellular
122 protein localization or cell–cell interactions.

123 Cellpose utilizes a neural network that is trained on ground-truth examples to
124 transform an input image into several intermediate outputs, including a scalar probability
125 field for identifying cell pixels (Extended Data Fig. 3a, panels *i-iii*)¹². Cellpose is unique
126 among DNN algorithms by the addition of a vector field output, which is defined by the
127 normalized gradient of a heat distribution from the median cell pixel coordinate
128 (Extended Data Fig. 3a, panels *iv,v*). This vector field directs pixels toward a global cell
129 center via Euler integration, allowing cells to be segmented based on the points at which
130 pixels coalesce (Extended Data Fig. 3b). In contrast to other algorithms, this approach for

131 reconstructing cells is size- and morphology-independent, insofar as the cell center can be
132 correctly defined.

133 To further interrogate the accuracy of Cellpose on our dataset, we evaluated its
134 performance as a function of cell size. We compared cell area against the number of
135 segmentation errors, calculated as the number of redundant or missing masks
136 corresponding to each ground-truth cell mask. This revealed a strong correlation between
137 cell size and segmentation errors, with the top quartile of cells accounting for 83% of all
138 errors (Fig. 2a). To understand the source of these errors, we inspected the flow field
139 output of many poorly segmented cells across a variety of species and growth conditions.
140 This showed that elongated cells, an important morphology often seen in both wild-type
141 and mutant bacterial populations, are particularly susceptible to over-segmentation (Fig.
142 2b). We attribute this to the multiple sinks apparent in the corresponding flow fields. In
143 the Cellpose mask reconstruction algorithm, pixels belonging to these cells are guided
144 into multiple centers per cell, fragmenting the cell into many separate masks.

145 We hypothesized that the observed defect in Cellpose flow field output is a
146 consequence of two distinct flow field types arising from our training dataset: those
147 where the median pixel coordinate, or ‘center’, lies within the cell (97.8%) and those
148 where it lies outside the cell (2.2%). In the latter, Cellpose projects the center point to the
149 nearest boundary pixel, ultimately leading to points of negative divergence on the cell
150 periphery that are chaotically distributed (Fig. 2c-e). On the contrary, non-projected
151 centers maintain a uniform field magnitude along the entire boundary and adhere to the
152 global symmetries of the cell (Extended Data Fig. 4a,d). A similar issue is also
153 encountered in cells with centers that are not projected but lie close to the boundary

154 (Extended Data Fig. 4b-d). Cells with a center point closer than 0.3 times the mean cell
155 diameter (a factor of 0.2 off-center) to the boundary account for an additional 8.5% of our
156 data. Neural networks can be exquisitely sensitive to the outliers in their training data³²;
157 therefore, we suspect that this small fraction of corrupt flow fields has significantly
158 impacted the performance of Cellpose.

159

160 **Development of a new DNN-based segmentation algorithm**

161 As there exists no straightforward means of defining a cell center for irregular
162 objects, we sought to develop a segmentation algorithm that operates independently of
163 cell center identification. We built our new algorithm, which we named Omnipose,
164 around the scalar potential known as the distance field (or distance transform), which
165 describes the distance at any point \vec{x} in a bounded region Ω to the closest point on the
166 boundary $\partial\Omega$. Notably, this widely utilized construct is one of the intermediate outputs of
167 StarDist³². Whereas in StarDist it is used to seed and assemble star-convex polygons, its
168 use in Omnipose is to define a new flow field within the Cellpose framework. The use of
169 a distance field has several advantages. First, the distance field is defined by the eikonal
170 equation $|\vec{\nabla}\Phi(\vec{x})| = 1$, and so its gradient has unit magnitude throughout the bounded
171 region for which it is calculated. This grants it faster convergence and better numerical
172 stability when compared to alternative solutions producing similar fields (*e.g.*, screened
173 Poisson; see Methods) (Extended Data Fig. 5a). Second, the distance field is independent
174 of morphology and topology, meaning that it is applicable to all cells. Lastly, the
175 resulting flow field points uniformly from cell boundaries toward the local cell center,
176 coinciding with the medial axis, or skeleton, that is defined by the stationary points of the

177 distance field (Extended Data Fig. 5b). This critical feature allows pixels to remain
178 spatially clustered after Euler integration, solving the problem of over-segmentation seen
179 in Cellpose.

180 One challenge to using the distance field as the basis to our approach is that
181 traditional distance field algorithms like FMM (Fast Marching Method) are sensitive to
182 boundary pixilation³³, causing artifacts in the flow field that extend deep into the cell.
183 These artifacts are sensitive to pixel-scale changes at the cell perimeter, which we
184 reasoned would interfere with the training process. To solve this, we developed an
185 alternative approach based on FIM (Fast Iterative Method) that produces smooth distance
186 fields for arbitrary cell shapes and sizes (Fig. 3a, and see Methods)³⁴. The corresponding
187 flow field is relatively insensitive to boundary features at points removed from the cell
188 boundary, a critical property for robust and generalized prediction by the Cellpose
189 network.

190 The use of the distance field additionally required a unique solution for mask
191 reconstruction. Whereas the pixels in a center-seeking field converge on a point, standard
192 Euler integration under our distance-derived field tends to cluster pixels into multiple thin
193 fragments along the skeleton, causing over-segmentation (Fig. 3b). We solved this with a
194 suppression factor of $(t + 1)^{-1}$ in each time step of the Euler integration. This reduces
195 the movement of each pixel after the first step $t = 0$, facilitating initial cell separation
196 while preventing pixels from clustering into a fragmented skeleton formation. The wider
197 distribution resulting from our suppression factor allows pixels to remain connected,
198 thereby generating a single mask for each cell in conjunction with a standard automated
199 pixel clustering algorithm (*e.g.*, DBSCAN)³⁵.

200

201 **Omnipose demonstrates unprecedented segmentation accuracy of bacterial cells**

202 With solutions to the major challenges of cell center-independent segmentation
203 incorporated into Omnipose, we proceeded to benchmark its performance. Remarkably,
204 across the IoU threshold range 0.5-1.0, Omnipose averages a JI >10-fold above that of
205 Cellpose (Fig. 4a). The difference in performance between the algorithms is particularly
206 pronounced within the high IoU range (0.75-1.0), where we observe an average of 170-
207 fold higher JI for Omnipose. At the 0.5-5 μm scale and with a typical microscope
208 configuration, quantitative measurements rely upon IoU values in this range, thus
209 Omnipose is uniquely suited for the microscopic analysis of bacterial cells.

210 To dissect the contributions of the individual Omnipose innovations to the overall
211 performance of the algorithm, we isolated the mask reconstruction component of
212 Omnipose and applied it to the Cellpose network output. This augmentation of Cellpose
213 modestly improved its performance to a roughly equivalent extent across all IoU
214 thresholds (Fig. 4a). Based on this, we attribute the remaining gains in performance by
215 Omnipose to its unique network outputs and our improvements to the Cellpose training
216 framework (see Methods).

217 Our analyses illuminated critical flaws in prior DNN-based approaches for the
218 segmentation of elongated cells, effectively preventing these algorithms from
219 generalizable application to bacteria (Fig. 1). To determine whether Omnipose overcomes
220 this limitation, we evaluated its performance as a function of cell area. Cell area serves as
221 a convenient proxy for cell length in our dataset, which is composed of both branched
222 and unbranched elongated cells. Whereas the Cellpose cell error rate remains above 9%

223 and increases exponentially with cell size, Omnipose displays a consistent error rate that
224 remains below 4% for all percentiles (Fig. 4b). Thus, Omnipose performance is
225 independent of cell size and shape, including those cells with complex, extended
226 morphologies (Fig. 4c,d).

227

228 **Omnipose permits sensitive detection of cellular intoxication**

229 Our laboratory recently described an interbacterial type VI secretion system-
230 delivered toxin produced by *Serratia proteamaculans*, Tre1³⁶. We showed that this toxin
231 acts by ADP-ribosylating the essential cell division factor FtsZ; however, we were unable
232 to robustly evaluate the consequences of Tre1 intoxication on target cell morphology
233 owing to segmentation challenges. Here we asked whether Omnipose could permit
234 straightforward and sensitive detection of intoxication by Tre1. To this end, we incubated
235 *S. proteamaculans* wild-type or a control strain expressing inactive Tre1 (*tre1*^{E415Q}) with
236 target *E. coli* cells and imaged these mixtures after a fixed period of 20 hours. Owing to
237 the unique capabilities of Omnipose, we were able to include dense fields of view,
238 incorporating >300,000 cells in our analysis.

239 Among the cells identified by Omnipose, we found a small proportion were
240 elongated and much larger than typical bacteria (Fig. 5a,b and Extended Data Fig. 6a).
241 These cells were only detected in mixtures containing active Tre1, and the apparent
242 failure of the cells to septate is consistent with the known FtsZ-inhibitory activity of the
243 toxin. The *S. proteamaculans* strain background we employed in this work expresses the
244 green fluorescent protein. Corresponding fluorescence images allowed us to
245 unambiguously assign the enlarged cell population to *E. coli* (Fig. 5c). Next, we

246 subjected the same images to cell segmentation with StarDist, Cellpose, and MiSiC, the
247 three top-performing algorithms in our initial survey. Each of these algorithms fail to
248 identify this population of cells to high precision (Fig. 5d,e). Close inspection reveals
249 three distinct modes of failure (Fig. 5e and Extended Data Fig. 6b). In the case of
250 StarDist, elongated (non-star-convex) cells are split into multiple star-convex subsets that
251 do not span the entire cell. Cellpose detects entire elongated cells, but it breaks them up
252 into a multitude of smaller masks. Conversely, MiSiC detects all cells but fails to
253 properly separate them, thereby exaggerating the area measurement in many cases. Taken
254 together, these data illustrate how the enhanced cell segmentation performance of
255 Omnipose can facilitate unique insights into microbiological systems.

256

257 **Omnipose exhibits strong performance in non-bacterial segmentation tasks**

258 We have shown that the features we developed within Omnipose improved phase-
259 contrast bacterial segmentation performance beyond that of Cellpose. However, it is
260 possible that these features could hinder performance relative to Cellpose in other
261 imaging modalities or in segmentation tasks involving, for example, eukaryotic cells,
262 whole organisms, and cell-like objects. To test this, we trained Omnipose on the cyto2
263 dataset, a large collection of images and corresponding ground-truth annotations
264 submitted by users that expands upon the original cyto dataset of Cellpose^{12,30}. We found
265 that Omnipose offers a modest improvement in performance relative to Cellpose on this
266 dataset (Fig. 5f and Extended Data Fig. 7a). Moreover, Omnipose achieved this
267 performance boost without compromising the segmentation rate (~1 image per second).

268 Encouraged by the strong performance of Omnipose on the cyto2 dataset, we next
269 sought to investigate its potential utility in a field far removed from microbiology. The
270 nematode *Caenorhabditis elegans* is a widely studied model organism with an overall
271 morphology grossly similar to elongated bacteria³⁷. At just one millimeter in length,
272 intact *C. elegans* are often analyzed by microscopy in order to measure phenotypes;
273 therefore, there is significant interest in methods for their accurate segmentation to enable
274 tracking³⁸. We obtained, annotated and trained Omnipose on two publicly available
275 microscopy datasets composed of *C. elegans* images: time-lapse frames from the Open
276 Worm Movement database³⁹ and frames containing fields of assorted live or dead *C.*
277 *elegans* from the BBBC010 dataset⁴⁰. These images contain debris and are of
278 heterogenous quality, yet 82% of masks predicted by Omnipose match or exceed the 0.8
279 IoU threshold (Fig. 5g,h). Taken together with our findings on cyto2, we conclude that
280 Omnipose inherits and offers improvement upon the broad applicability of Cellpose.

281

282 **Discussion**

283 Confronted with the importance of segmentation accuracy to the success of work
284 within our own laboratory, we were motivated to characterize the performance of several
285 existing cell segmentation algorithms. Recent developments in deep learning have greatly
286 improved these algorithms; however, significant challenges remain^{1,30}. Although isolated
287 cells without cell-to-cell contact can be segmented with high precision by any of the
288 packages we tested, segmentation becomes significantly more challenging when cells
289 form microcolonies, adopt irregular morphologies, or when fields are composed of cells
290 with multiple shapes and sizes. Such difficulties are compounded in time-lapse studies,

291 where the significance of segmentation errors often grows exponentially with time.
292 Experimental design can help mitigate certain segmentation challenges; however, the
293 recent emphasis on non-model organisms and microbial communities renders this an
294 increasingly undesirable solution⁴¹.

295 This work provides the most comprehensive side-by-side quantitative comparison
296 of cell segmentation algorithm performance to-date. As expected, machine-learning-
297 based approaches outperform others, yet insights into general image segmentation
298 strategies can be gained from each of the methods we examined. Two of the six
299 algorithms we tested utilize traditional image thresholding and watershed segmentation:
300 Morphometrics and SuperSegger^{13,23}. Each program tends to under-segment adjacent
301 cells and over-segment large cells, behaviors previously linked to thresholding and
302 watershed processes, respectively^{1,42}. Given that SuperSegger was motivated at least in-
303 part to mitigate these issues, we postulate that traditional image segmentation approaches
304 are ultimately limited to specialized imaging scenarios. Although we classify MiSiC as a
305 DNN-based approach, this algorithm also relies on thresholding and watershed
306 segmentation to generate cell masks from its network output¹⁵. The network output of
307 MiSiC is more uniform than unfiltered phase contrast images, yet this pre-processing
308 does not fully abrogate the typical errors of thresholding and watershed segmentation.
309 We therefore conclude that, even when combined with neural networks as seen in MiSiC,
310 thresholding and watershed cannot be effectively used for general cell segmentation
311 tasks.

312 A successful DNN-based algorithm is composed of a robust, consistent neural
313 network output, and an appropriate mask reconstruction process based on this output. In

314 the case of Mask R-CNN, bounding boxes for each cell are predicted along with a
315 probability field that localizes a cell within its bounding box⁴³. Masks are generated by
316 iterating over each box and thresholding the probability field. Despite the widespread
317 adoption of Mask R-CNN, we found this algorithm did not perform exceptionally well in
318 our study. Our results suggest that this is due to dense cell fields with overlapping
319 bounding boxes, a feature known to corrupt the training process and produce poor
320 network outputs for Mask R-CNN⁴⁴. By contrast, the StarDist network makes robust
321 predictions, but it fails to assemble accurate cell masks because the cells in our dataset
322 are not well approximated by star-convex polygons²⁶. The errors we encountered with
323 Cellpose can be attributed to both neural network output and mask reconstruction. In
324 Omnipose, we specifically addressed these two issues via the distance field and
325 suppressed Euler integration, respectively, yielding a remarkably precise and
326 generalizable image segmentation tool. Omnipose effectively leverages the strongest
327 features of several of the DNN approaches we tested, namely the distance field of
328 StarDist, the boundary field of MiSiC, and the mask reconstruction framework of
329 Cellpose.

330 We have designed Omnipose for use by typical research laboratories and we have
331 made its source code and training data publicly available. For images of bacteria under
332 phase contrast, researchers will not need to provide new ground truth data or retrain the
333 model. In this study, we emphasized morphological diversity, but we further accounted
334 for differences in optical features between bacterial strains, slide preparation techniques,
335 and microscope configurations. For example, the images in our ground-truth dataset
336 originate from four different researchers using distinct microscopes, objectives, sensors,

337 illumination sources, and acquisition settings. We further introduced extensive image
338 augmentations that simulate variations in image intensity, noise, gamma, clipping, and
339 magnification. Lastly, bacterial strains exhibit a wide range of intrinsic contrast and
340 internal structure, often exacerbated by antibiotic treatment or revealed by dense cell
341 packing. Internal structure can cause over-segmentation, so we included many cells with
342 this characteristic in our dataset.

343 We anticipate that the unprecedented performance of Omnipose may permit
344 access to information from microscopy images that was previously inaccessible. For
345 instance, images deriving from natural microbial communities could be accurately
346 characterized with regard to internal structure, autofluorescence, and morphology at the
347 single-cell level. This data could be used to estimate diversity, a novel methodology that
348 would complement existing sequencing-based metrics⁴⁵. It is worth noting that
349 phenotypic diversity often exceeds genetic diversity⁴⁶; therefore, even in a relatively
350 homogeneous collection of organisms, precise segmentation could allow classes
351 representing distinct states to be identified. A microscopy-based approach also offers the
352 opportunity to characterize spatial relationships between cells, information that is
353 exceptionally difficult to recover in most biomolecular assays.

354 **Methods**

355 **Phase contrast and fluorescence microscopy**

356 In-house imaging was performed on a Nikon Eclipse Ti-E wide-field epi-
357 fluorescence microscope, equipped with a sCMOS camera (Hamamatsu) and X-cite LED
358 for fluorescence imaging. We imaged through 60X and 100X 1.4 NA oil-immersion PH3
359 objectives. The microscope was controlled by NIS-Elements. Cell samples were spotted
360 on a 3% (w/v) agarose pad placed on a microscope slide. The microscope chamber was
361 heated to 30°C or 37°C when needed for time-lapse experiments.

362 Several images in our dataset were taken by two other laboratories using three
363 distinct microscope/camera configurations. The Brun lab provided images of *C.*
364 *crescentus* acquired on a Nikon Ti-E microscope equipped with a Photometrics Prime
365 95B sCMOS camera. Images were captured through a 60X Plan Apo λ 100X 1.45 NA oil
366 Ph3 DM objective. The Wiggins lab provided *E. coli* and *A. baylyi* time lapses from both
367 a Nikon Ti-E microscope as well as a custom-built tabletop microscope, both described in
368 previous studies^{47,48}.

369

370 ***C. elegans* data preparation**

371 We obtained a 1000-frame time lapse of *C. elegans* from the Wormpose³⁸ GitHub
372 (https://github.com/iteal/wormpose_data) adapted from the Open Worm Movement
373 database³⁹, which is inaccessible at the time of writing. We also utilized the Broad
374 Bioimage Benchmarking Collection set BBBC010⁴⁰ ([https://bbbc.broadinstitute.org/c-](https://bbbc.broadinstitute.org/c-elegans-livedead-assay-0)
375 *elegans-livedead-assay-0*), a set of 100 images containing live and dead *C. elegans*.
376 These images were manually cropped to select regions of each image without *C. elegans*

377 overlaps. For both of these datasets, images were initially segmented with Omnipose to
378 select foreground, automatically cropped to select individual *C. elegans* or clusters of *C.*
379 *elegans*, and then packed into ensemble images for efficient annotation, training, and
380 testing following the same procedures described below for our bacterial datasets.

381

382 **Bacterial sample preparation**

383 To image antibiotic-induced phenotypes, cells were grown without antibiotics
384 overnight in LB, back-diluted, and spotted on agarose pads with 50µg/mL A22 or
385 10µg/mL cephalexin. Time lapses were captured of *E. coli* DH5α and *S. flexneri* M90T
386 growing on these pads. *E. coli* CS703-1 was back-diluted into LB containing 1µg/mL
387 aztreonam and spotted onto a pad without antibiotics⁴⁹. Cells constitutively expressed
388 GFP to visualize cell boundaries.

389 *H. pylori* LSH100 grown with and without Aztreonam was provided by the
390 Salama lab^{50,51}. Samples were fixed and stained with Alexafluor 488 to visualize the cell
391 membrane. Images were taken on LB pads. The typical technique of allowing the spot to
392 dry on the pad caused cells to curl up on themselves, so our images were taken by placing
393 the cover slip on the pad immediately after spotting and applying pressure to force out
394 excess media.

395 *C. crescentus* was cultivated and imaged by the Brun lab^{52,53}. Cells were grown in
396 PYE, washed twice in water prior to 1:20 dilution in Hutner base-imidazole-buffered-
397 glucose-glutamate (HIGG media) and grown at 26°C for 72h. Cells were spotted on a 1%
398 agarose PYE pads prior to imaging.

399 *S. pristinaespiralis* NRRL 2958 was grown using the following media recipe:
400 Yeast extract 4g/L, Malt extract 10g/L, Dextrose 4g/L, Agar 20g/L. This media was used
401 to first culture the bacteria in liquid overnight and then on a pad under the microscope.
402 This strain forms aggregates in liquid media, so these aggregates were allowed to grow
403 for several hours on a slide in the heated microscope chamber until we could see
404 individual filaments extending from the aggregates. Fields of view were selected and
405 cropped to exclude cell overlaps. Autofluorescence was captured to aid in manual
406 segmentation.

407 Mixtures of *S. proteamaculans* attTn7::Km-gfp *tre1* or *tre1*^{E415Q} and *E. coli* were
408 spotted on a PBS pad to prevent further growth. Phase-contrast images of the cells were
409 acquired before and after a 20hr competition on a high-salt LB plate. Fluorescence
410 images in the GFP channel were also acquired to distinguish *S. proteamaculans* from
411 unlabeled *E. coli*.

412 All other individual strains in Table S1 were grown overnight, diluted 1:100 into
413 fresh LB media, and grown for 1-3 hours before imaging. Mixtures were made by
414 combining back-diluted cells roughly 1:1 by OD₆₀₀.

415

416 **Manual image annotation**

417 Manual annotation began with loading images into MATLAB, normalizing the
418 channels, registering the fluorescence channel(s) to brightfield (when applicable), and
419 producing boundary-enhanced versions of brightfield and fluorescence. Where possible,
420 fluorescence data was primarily used to define cell boundaries (not available in the *C.*
421 *elegans* dataset acquired online). In addition to a blank channel to store manual labels, all

422 processed phase and fluorescence images were then automatically loaded as layers into
423 an Adobe Photoshop document. We used 4-6 unique colors and the Pencil tool (for pixel-
424 level accuracy and no blending) to manually define object masks. Due to the 4-color
425 theorem⁵⁴, this limited palette was sufficient to clearly distinguish individual object
426 instances from each other during annotation. This color simplification is not found in any
427 segmentation GUI, and it enabled faster manual annotation by reducing the need to select
428 new colors. It also eliminated the confusion caused by the use of similar but distinct
429 colors in adjacent regions, which we suspect is the principal cause for the misplaced
430 mask pixels that we observed in other datasets (*e.g.*, cyto2).

431 The cell label layer was then exported as a PNG from Photoshop, read back into
432 MATLAB, and converted from the repeating N-color labels to a standard 16-bit integer
433 label matrix, where each object is assigned a unique integer from 1 to the number of cells
434 (background is 0). Because integer labels cannot be interpolated, we then performed a
435 non-rigid image registration of the brightfield channel to the binary label mask to achieve
436 better brightfield correlation to ground truth masks. All images in our ground-truth
437 dataset have been registered in this manner.

438

439 **Choosing Segmentation algorithms**

440 Three main factors contributed to the choice of algorithms highlighted in this
441 study: (*i*) specificity to bacterial phase contrast images, (*ii*) success and community
442 adoption, especially for bioimage segmentation, and (*iii*) feasibility of installation,
443 training, and use. SuperSegger, Morphometrics, and MiSiC were selected because they
444 specifically targeted the problem of bacterial phase contrast segmentation^{15,23,55}. Packages

445 such as BactMAP, BacStalk, Cellprofiler, CellShape, ColiCoords, Cytokit,
446 MicroAnalyzer, MicrobeJ, Oufiti, and Schnitzcells incorporate limited novel segmentation
447 solutions and instead aim to provide tools for single-cell analysis such as lineage tracing
448 and protein tracking^{8,9,14,18-20,25,56-58}. Furthermore, the segmentation that these programs
449 perform depends broadly on thresholding and watershed techniques; therefore,
450 Morphometrics is a reasonable proxy for their segmentation capabilities. We were unable
451 to locate code or training data for BASCA¹¹. Ilastik is a popular interactive machine-
452 learning tool for bioimage segmentation, but training it using a manual interface was not
453 feasible on a large and diverse dataset such as our own²¹. Among DNN approaches, Mask
454 R-CNN was selected because it is a popular architecture for handling typical image
455 segmentation tasks. It was also used in the segmentation and tracking package Usiigaci²⁴.
456 U-Net architectures have been implemented in a number of algorithms, including
457 DeLTA, PlantSeg, MiSiC, StarDist, and Cellpose^{12,15,17,22,26}. DeLTA was not included in
458 this study because it operates similarly to MiSiC and was designed specifically for
459 mother machine microfluidics analysis. DeLTA 2.0 was recently released to additionally
460 segment confluent cell growth on agarose pads, but it remains quite similar to MiSiC in
461 implementation⁵⁹. PlantSeg could, in principle, be trained on bacterial micrographs, but
462 we determined that its edge-focused design meant to segment bright plant cell wall
463 features would not offer any advancements over the remaining U-Net methods that we
464 tested.

465

466 **Training and tuning segmentation algorithms**

467 All segmentation algorithms have tunable parameters to optimize performance on
468 a given dataset. These include pre-processing such as image rescaling (often to put cells
469 into a particular pixel diameter range), contrast adjustment, smoothing, and noise
470 addition. Morphometrics and SuperSegger were manually tuned to give the best results
471 on our benchmarking dataset. The neural network component of SuperSegger was not
472 retrained on our data, as this is a heavily manual process involving toggling watershed
473 lines on numerous segmentation examples. DNN-based algorithms are automatically
474 trained using our dataset, and the scripts we used to do so are available in our GitHub
475 repository. We adapted our data for MiSiC by transforming our instance labels into
476 interior and boundary masks. Training documentation for MiSiC is not published.
477 Training and evaluation parameters for MiSiC were tuned according to correspondence
478 with the MiSiC authors. Cellpose and StarDist were trained with the default parameters
479 provided in their documentation. StarDist has an additional tool to optimize image pre-
480 processing parameters on our dataset, which we utilized.

481

482 **Evaluating segmentation algorithms**

483 All algorithms were evaluated on our benchmarking dataset with manually or
484 automatically optimized parameters. We provide both the raw segmentation results for all
485 test images by each tested algorithm as well as the models and model-training scripts
486 required to reproduce our results. Before evaluating IoU or JI, small masks at image
487 boundaries were removed for both the ground-truth and predicted masks. IoU and JI are
488 calculated on a per-image basis and, where shown, are averaged with equal weighting
489 over the image set or field of view.

490 Our new metric, the number of segmentation errors per cell, was calculated by
491 first measuring the fraction of each predicted cell that overlaps with each ground truth
492 cell. A predicted cell is assigned to a ground-truth cell if the overlap ratio is ≥ 0.75 ,
493 meaning that at least three quarters of the predicted cell lies within the ground-truth cell.
494 If several predicted cells are matched to a ground-truth cell, the number of surplus
495 matches is taken to be the number of segmentation errors. If no cells are matched to a
496 ground-truth cell, then the error is taken to be 1.

497

498 **Leveraging Omnipose to accelerate manual annotation**

499 Omnipose was periodically trained on our growing dataset to make initial cell
500 labels. These were converted into an N-color representation and loaded into Photoshop
501 for manual correction. A subset of our cytosol GFP channels were sufficient for training
502 Omnipose to segment based on fluorescence, and the resulting trained model enabled
503 higher-quality initial cell labels for GFP-expressing samples than could be achieved from
504 intermediate phase contrast models (e.g., *V. cholerae*).

505

506 **Defining the Omnipose prediction classes**

507 Omnipose predicts four classes: two flow components, the distance field, and a
508 boundary field. Our distance field is found by solving the eikonal equation

509
$$|\vec{\nabla}\phi(\vec{x})| = \frac{1}{f(\vec{x})}$$

510 where f represents the speed at a point \vec{x} . The Godunov upwind discretization of the
511 eikonal equation is

$$512 \quad \left(\frac{\max(\phi_{i,j} - \min(\phi_{i-1,j}, \phi_{i+1,j}), 0)}{\Delta x} \right)^2 + \left(\frac{\max(\phi_{i,j} - \min(\phi_{i,j-1}, \phi_{i,j+1}), 0)}{\Delta y} \right)^2 = \frac{1}{f_{i,j}}$$

513 Our solution to this equation is based on the Improved FIM Algorithm 1.1 of³⁴, as
 514 follows. Our key contribution to this algorithm is the addition of ordinal sampling to
 515 boost both convergence and smoothness of the final distance field.

516 *2D update function for $\phi_{i,j}$ on a cartesian grid*

517 1. Find neighboring points for cardinal axes ($\Delta x = \Delta y = \delta$):

$$518 \quad \phi^{\min x} = \min(\phi_{i-1,j}, \phi_{i+1,j}), \quad \phi^{\min y} = \min(\phi_{i,j-1}, \phi_{i,j+1})$$

519 2. Find neighboring points for ordinal axes ($\hat{x} \cdot \hat{a} = \hat{y} \cdot \hat{b} = \frac{\sqrt{2}}{2}, \frac{\Delta a}{\Delta x} = \frac{\Delta b}{\Delta y} = \sqrt{2}\delta$):

$$520 \quad \phi^{\min a} = \min(\phi_{i-1,j-1}, \phi_{i+1,j+1}), \quad \phi^{\min b} = \min(\phi_{i+1,j-1}, \phi_{i-1,j+1})$$

521 3. Calculate update along cardinal axes:

$$522 \quad \text{if } |\phi^{\min x} - \phi^{\min y}| > \frac{\sqrt{2}\delta}{f_{i,j}}:$$

$$523 \quad U^{xy} = \min(\phi^{\min x}, \phi^{\min y}) + \frac{\delta}{f_{i,j}}$$

524 **else:**

$$525 \quad U^{xy} = \frac{1}{2} \left(\phi^{\min x} + \phi^{\min y} + \sqrt{2 \left(\frac{\delta}{f_{i,j}} \right)^2 - (\phi^{\min x} - \phi^{\min y})^2} \right)$$

526 4. Calculate update along ordinal axes:

$$527 \quad \text{if } |\phi^{\min a} - \phi^{\min b}| > \frac{2\delta}{f_{i,j}}:$$

$$528 \quad U^{ab} = \min(\phi^{\min a}, \phi^{\min b}) + \frac{\sqrt{2}\delta}{f_{i,j}}$$

529 **else:**

$$530 \quad U^{ab} = \frac{1}{2} \left(\phi^{\min a} + \phi^{\min b} + \sqrt{4 \left(\frac{\delta}{f_{i,j}} \right)^2 - (\phi^{\min a} - \phi^{\min b})^2} \right)$$

531 5. Update with geometric mean:

$$532 \quad \phi_{i,j} = \sqrt{U^{xy}U^{ab}}$$

533 This update rule is repeated until convergence (Extended Data Fig. 5). We take
534 $\delta = f_{i,j}$ to obtain the signed distance field used in Omnipose. The flow field components
535 are defined by the normalized gradient of this distance field ϕ . The boundary field is
536 defined by points satisfying $0 < \phi < 1$. For network prediction, the boundary map is
537 converted to the logits (inverse sigmoid) representation, such that points in the range
538 $[0,1]$ are mapped to $[-5,5]$. For consistent value ranges across prediction classes, the
539 flow components are multiplied by 5 and all background values of the distance field ($\phi =$
540 0) are set to -5 .

541

542 **Omnipose network architecture**

543 The DNN used for Omnipose is a minor modification of that used in Cellpose: a
544 U-net architecture with two residual blocks per scale, each with two convolutional
545 layers¹². Omnipose introduces a dropout layer before the densely connected layer⁶⁰,
546 which we incorporated into the shared Cellpose and Omnipose architecture moving
547 forward. However, Cellpose models utilized in this study are trained without dropout.

548

549 **Rescaling flow field by divergence**

550 During training, the ground truth data is augmented by a random affine
551 transformation. The original implementation, and the one which yields the best results,
552 linearly interpolates the transformed field. This reduces the magnitude of the otherwise
553 normalized field in regions of divergence, *i.e.*, at boundaries and skeletons. A
554 renormalized field (obtained either from the transformed field or as the normalized
555 gradient of the transformed heat distribution) often has artifacts at cell boundaries and

556 skeletons, so the interpolated field effectively reduces the influence of these artifacts on
557 training. We reason that this feature explains the superior performance of interpolated
558 field training over renormalized fields, despite the latter being the nominal goal of the
559 algorithm.

560 Pixels at cell boundaries, however, consequently do not move far (less than 1px)
561 under Euler integration due to the low magnitude of the predicted field at cell boundaries.
562 Our solution in Omnipose is to rescale the flow field by the magnitude of the divergence.
563 The divergence is most positive at the cell boundaries (where pixels need to move) and
564 most negative at cell skeletons (where pixels need to stop). We therefore rescale the
565 divergence from 0 to 1 and multiply the normalized flow field by this new magnitude
566 map. This forces boundary pixels of neighboring cells to quickly diverge and allow for
567 accurate pixel clustering to obtain the final segmentation.

568

569 **Novel diameter metric**

570 The size models of Cellpose are trained to estimate the average cell ‘diameter’,
571 taken to be the diameter of the circle of equivalent area:

$$572 \qquad d = 2R = 2 \sqrt{\frac{A}{\pi}} \qquad (*)$$

573 This metric as a basis for rescaling is problematic when cells are growing in
574 length but not width (Extended Data Fig. 7). Log-phase bacterial cell area grows
575 exponentially with time, and so too does the scale factor, eventually resulting in a
576 rescaled image that is too small for Cellpose to segment.

577 The average of the distance field, however, does not change for filamentous
578 bacteria, as the width – and therefore the distance to the closest boundary – remains
579 constant. To define a formula consistent with the previous definition in the case of a
580 circular cell, we consider mean of the distance field over the cell:

$$581 \quad \bar{\phi} = \frac{1}{\pi R^2} \int_0^{2\pi} \int_0^R (R - r)r dr d\theta = \frac{1}{\pi R^2} \left(\frac{\pi}{3} R^3 \right) = \frac{R}{3}$$

582 This allows us to define a new ‘effective diameter’ as

$$583 \quad d = 2R = 6\bar{\phi} \quad (**)$$

584 Aside from agreeing with the previous scaling method (*) for round
585 morphologies, this definition exhibits excellent consistency across time (Extended Data
586 Fig. 7). This consistency is also critical for training on datasets with wide distributions in
587 cell areas that require rescaling, such as the Cellpose datasets. Finally, the raw distance
588 field output of Omnipose can directly be used directly in (**) to estimate average cell
589 diameter, which is used in our code to automatically toggle on features that improve
590 mask reconstruction performance for small cells.

591

592 **Gamma augmentation**

593 To make the network robust against changes in exposure/contrast, the training
594 images are now raised to a random power (gamma) between 0.5 and 1.25, simulating the
595 varying levels of contrast that are observed experimentally with different light sources,
596 objectives, and exposure times.

597

598

599

600 **Alleviating class imbalance**

601 Class imbalance remains a challenge in many machine learning applications⁶¹. In
602 our dataset, foreground pixels (cells) take up anywhere from 1 to 75 percent of a given
603 training image, with the rest being background pixels that the network must only learn to
604 ignore (*i.e.*, assign a constant output of -5 for distance and boundary logits). We
605 implemented several changes to the loss function to emphasize foreground objects,
606 including weighting by the distance field and averaging some loss terms only over
607 foreground pixels. Our training augmentation function also attempts many random crop
608 and resizing passes until a field of view with foreground pixels is selected (this may take
609 several attempts for sparse images, but adds very little time to training).

610

611 **Image normalization**

612 To manage different image exposure levels, Cellpose automatically rescales
613 images such that pixels in the 1st percentile of intensity are set to 0 and those in the 99th
614 percentile are sent to 1. This percentile rescaling is preferred over blind min-max
615 rescaling because bubbles or glass can cause small bright spots in the image. However,
616 we found that images containing single cells (low intensity) in a wide field of media
617 (high intensity) would become badly clipped due to the foreground-background class
618 imbalance. To solve this, we changed the percentile range from 0.01 to 99.99.

619

620 **Data availability**

621 Ground truth images and labels generated for this study are hosted on the Cellpose
622 website (http://www.cellpose.org/dataset_omnipose) and listed on the Papers With Code
623 database (<https://paperswithcode.com/dataset/bpcis>).

624

625 **Code availability**

626 Python and MATLAB scripts generated for this study is available from GitHub at
627 <https://github.com/kevinjohncutler/omnipose>. Omnipose is available as part of the
628 Cellpose package at <https://github.com/mouseland/cellpose>.

629 **Acknowledgements**

630 The authors wish to thank members of the Mougous and Wiggins laboratories for helpful
631 suggestions, See-Yeun Ting for assistance with experiments, Teresa Lo for assistance
632 with image acquisition, Sophie Sichel and Nina Salama lab for growing, fixing, and
633 staining *H. pylori* samples for in-house imaging, and David Kysela, Maxime Jacq and
634 Yves Brun for providing *C. crescentus* images. This work was supported by the NIH
635 (AI080609 to JDM, GM128191 to PAW, T32GM008268 to KJC). JDM is an HHMI
636 Investigator.

637

638 **Competing interests**

639 The authors declare no competing interests.

640

641 **Author contributions**

642 KJC, PAW and JDM conceived the study. KJC performed experiments, analyzed data,
643 and wrote the code. KJC, PAW, and JDM wrote the manuscript. CS edited the
644 manuscript and assisted in code development.

645

646 **Author Information**

647 Correspondence and requests for materials should be addressed to J.D.M.

648 (mougous@u.washington.edu) or P.A.W. (pwiggins@uw.edu).

649

650 References

- 651 1 Jeckel, H. & Drescher, K. Advances and opportunities in image analysis of
652 bacterial cells and communities. *FEMS Microbiol Rev* **45**,
653 doi:10.1093/femsre/fuaa062 (2021).
- 654 2 Bali, A. & Singh, S. N. in *IEEE Xplore* 113-120 (IEEE, 2015).
- 655 3 Lucas, A. M. *et al.* Open-source deep-learning software for bioimage
656 segmentation. *Mol Biol Cell* **32**, 823-829, doi:10.1091/mbc.E20-10-0660 (2021).
- 657 4 Kysela, D. T., Randich, A. M., Caccamo, P. D. & Brun, Y. V. Diversity Takes
658 Shape: Understanding the Mechanistic and Adaptive Basis of Bacterial
659 Morphology. *PLoS Biol* **14**, e1002565, doi:10.1371/journal.pbio.1002565 (2016).
- 660 5 Jones, S. E. & Elliot, M. A. 'Exploring' the regulation of *Streptomyces* growth and
661 development. *Curr Opin Microbiol* **42**, 25-30, doi:10.1016/j.mib.2017.09.009
662 (2018).
- 663 6 Caccamo, P. D. & Brun, Y. V. The Molecular Basis of Noncanonical Bacterial
664 Morphology. *Trends Microbiol* **26**, 191-208, doi:10.1016/j.tim.2017.09.012
665 (2018).
- 666 7 Behera, B. *et al.* Emerging technologies for antibiotic susceptibility testing.
667 *Biosens Bioelectron* **142**, 111552, doi:10.1016/j.bios.2019.111552 (2019).
- 668 8 Paintdakhi, A. *et al.* Oufiti: an integrated software package for high-accuracy,
669 high-throughput quantitative microscopy analysis. *Molecular microbiology* **99**,
670 767-777, doi:10.1111/mmi.13264 (2016).
- 671 9 Ducret, A., Quardokus, E. M. & Brun, Y. V. MicrobeJ, a tool for high throughput
672 bacterial cell detection and quantitative analysis. *Nat Microbiol* **1**, 16077,
673 doi:10.1038/nmicrobiol.2016.77 (2016).
- 674 10 Tropini, C., Earle, K. A., Huang, K. C. & Sonnenburg, J. L. The Gut Microbiome:
675 Connecting Spatial Organization to Function. *Cell Host Microbe* **21**, 433-442,
676 doi:10.1016/j.chom.2017.03.010 (2017).
- 677 11 Balomenos, A. D. *et al.* Image analysis driven single-cell analytics for systems
678 microbiology. *BMC Syst Biol* **11**, 43, doi:10.1186/s12918-017-0399-z (2017).
- 679 12 Stringer, C., Wang, T., Michaelos, M. & Pachitariu, M. Cellpose: a generalist
680 algorithm for cellular segmentation. *Nature methods* **18**, 100-106,
681 doi:10.1038/s41592-020-01018-x (2021).
- 682 13 Stylianidou, S., Brennan, C., Nissen, S. B., Kuwada, N. J. & Wiggins, P. A.
683 SuperSegger: robust image segmentation, analysis and lineage tracking of

- 684 bacterial cells. *Molecular microbiology* **102**, 690-700, doi:10.1111/mmi.13486
685 (2016).
- 686 14 van Raaphorst, R., Kjos, M. & Veening, J. W. BactMAP: An R package for
687 integrating, analyzing and visualizing bacterial microscopy data. *Molecular*
688 *microbiology* **113**, 297-308, doi:10.1111/mmi.14417 (2020).
- 689 15 Panigrahi, S. *et al.* Misic, a general deep learning-based method for the high-
690 throughput cell segmentation of complex bacterial communities. *Elife* **10**,
691 doi:10.7554/eLife.65151 (2021).
- 692 16 Bannon, D. *et al.* DeepCell Kiosk: scaling deep learning-enabled cellular image
693 analysis with Kubernetes. *Nature methods* **18**, 43-45, doi:10.1038/s41592-020-
694 01023-0 (2021).
- 695 17 Lugagne, J. B., Lin, H. & Dunlop, M. J. DeLTA: Automated cell segmentation,
696 tracking, and lineage reconstruction using deep learning. *PLoS computational*
697 *biology* **16**, e1007673, doi:10.1371/journal.pcbi.1007673 (2020).
- 698 18 Smit, J. H., Li, Y., Warszawik, E. M., Herrmann, A. & Cordes, T. ColiCoords: A
699 Python package for the analysis of bacterial fluorescence microscopy data. *PLoS*
700 *One* **14**, e0217524, doi:10.1371/journal.pone.0217524 (2019).
- 701 19 Czech, E., Aksoy, B. A., Aksoy, P. & Hammerbacher, J. Cytokit: a single-cell
702 analysis toolkit for high dimensional fluorescent microscopy imaging. *BMC*
703 *Bioinformatics* **20**, 448, doi:10.1186/s12859-019-3055-3 (2019).
- 704 20 McQuin, C. *et al.* CellProfiler 3.0: Next-generation image processing for biology.
705 *PLoS Biol* **16**, e2005970, doi:10.1371/journal.pbio.2005970 (2018).
- 706 21 Berg, S. *et al.* ilastik: interactive machine learning for (bio)image analysis. *Nature*
707 *methods* **16**, 1226-1232, doi:10.1038/s41592-019-0582-9 (2019).
- 708 22 Wolny, A. *et al.* Accurate and versatile 3D segmentation of plant tissues at
709 cellular resolution. *Elife* **9**, doi:10.7554/eLife.57613 (2020).
- 710 23 Ursell, T. *et al.* Rapid, precise quantification of bacterial cellular dimensions
711 across a genomic-scale knockout library. *BMC Biol* **15**, 17, doi:10.1186/s12915-
712 017-0348-8 (2017).
- 713 24 Tsai, H. F., Gajda, J., Sloan, T. F. W., Rares, A. & Shen, A. Usiigaci: Instance-
714 aware cell tracking in stain-free phase contrast microscopy enabled by machine
715 learning. *SoftwareX* **9**, 230-237, doi:<https://doi.org/10.1016/j.softx.2019.02.007>
716 (2019).
- 717 25 Reiner, J., Azran, G. & Hyams, G. MicroAnalyzer: A Python Tool for Automated
718 Bacterial Analysis with Fluorescence Microscopy. *arXiv*,
719 doi:<https://arxiv.org/abs/2009.12684> (2020).

- 720 26 Schmidt, U. *et al.* *Cell Detection with Star-Convex Polygons*. (2018).
- 721 27 He, K., Gkioxari, G., Dollar, P. & Girshick, R. Mask R-CNN. *arXiv*,
722 doi:<https://arxiv.org/abs/1703.06870> (2018).
- 723 28 Shal, K. & Choudhry, M. S. Evolution of Deep Learning Algorithms for MRI-
724 Based Brain Tumor Image Segmentation. *Crit Rev Biomed Eng* **49**, 77-94,
725 doi:10.1615/CritRevBiomedEng.2021035557 (2021).
- 726 29 Bean, G. J. *et al.* A22 disrupts the bacterial actin cytoskeleton by directly binding
727 and inducing a low-affinity state in MreB. *Biochemistry* **48**, 4852-4857,
728 doi:10.1021/bi900014d (2009).
- 729 30 Laine, R. F., Arganda-Carreras, I., Henriques, R. & Jacquemet, G. Avoiding a
730 replication crisis in deep-learning-based bioimage analysis. *Nature methods* **18**,
731 1136-1144, doi:10.1038/s41592-021-01284-3 (2021).
- 732 31 Taha, A. A. & Hanbury, A. Metrics for evaluating 3D medical image
733 segmentation: analysis, selection, and tool. *BMC Med Imaging* **15**, 29,
734 doi:10.1186/s12880-015-0068-x (2015).
- 735 32 Lu, W. *et al.* Unsupervised Sequential Outlier Detection With Deep Architectures.
736 *IEEE Trans Image Process* **26**, 4321-4330, doi:10.1109/TIP.2017.2713048
737 (2017).
- 738 33 Sethian, J. A. & Vladimirsky, A. Ordered upwind methods for static Hamilton-
739 Jacobi equations. *Proc Natl Acad Sci U S A* **98**, 11069-11074,
740 doi:10.1073/pnas.201222998 (2001).
- 741 34 Huang, Y. Improved Fast Iterative Algorithm for Eikonal Equation for GPU
742 Computing. *arXiv*, doi:<http://arXiv:2106.15869v3> (2021).
- 743 35 Ester, M., Kreigel, H. P., Sander, J. & Xu, X. A density-based algorithm for
744 discovering clusters in large spatial databases with noise. doi:10.1.1.121.9220
745 (1996).
- 746 36 Ting, S. Y. *et al.* Bifunctional Immunity Proteins Protect Bacteria against FtsZ-
747 Targeting ADP-Ribosylating Toxins. *Cell* **175**, 1380-1392,
748 doi:10.1016/j.cell.2018.09.037 (2018).
- 749 37 Girard, L. R. *et al.* WormBook: the online review of *Caenorhabditis elegans*
750 biology. *Nucleic Acids Res* **35**, D472-475, doi:10.1093/nar/gkl894 (2007).
- 751 38 Hebert, L., Ahamed, T., Costa, A. C., O'Shaughnessy, L. & Stephens, G. J.
752 WormPose: Image synthesis and convolutional networks for pose estimation in *C.*
753 *elegans*. *PLoS computational biology* **17**, e1008914,
754 doi:10.1371/journal.pcbi.1008914 (2021).

- 755 39 Javer, A. *et al.* An open-source platform for analyzing and sharing worm-behavior
756 data. *Nature methods* **15**, 645-646, doi:10.1038/s41592-018-0112-1 (2018).
- 757 40 Ljosa, V., Sokolnicki, K. L. & Carpenter, A. E. Annotated high-throughput
758 microscopy image sets for validation. *Nature methods* **9**, 637,
759 doi:10.1038/nmeth.2083 (2012).
- 760 41 Cusick, J. A., Wellman, C. L. & Demas, G. E. The call of the wild: using non-
761 model systems to investigate microbiome-behaviour relationships. *J Exp Biol* **224**,
762 doi:10.1242/jeb.224485 (2021).
- 763 42 Wang, Z. Cell Segmentation for Image Cytometry: Advances, Insufficiencies, and
764 Challenges. *Cytometry A* **95**, 708-711, doi:10.1002/cyto.a.23686 (2019).
- 765 43 He, C. *et al.* Genome-resolved metagenomics reveals site-specific diversity of
766 episymbiotic CPR bacteria and DPANN archaea in groundwater ecosystems. *Nat*
767 *Microbiol* **6**, 354-365, doi:10.1038/s41564-020-00840-5 (2021).
- 768 44 Looi, S. *rotated_maskrcnn*, <https://github.com/mrlooi/rotated_maskrcnn>
769 (2019).
- 770 45 Bharti, R. & Grimm, D. G. Current challenges and best-practice protocols for
771 microbiome analysis. *Brief Bioinform* **22**, 178-193, doi:10.1093/bib/bbz155
772 (2021).
- 773 46 Smits, W. K., Kuipers, O. P. & Veening, J. W. Phenotypic variation in bacteria:
774 the role of feedback regulation. *Nat Rev Microbiol* **4**, 259-271,
775 doi:10.1038/nrmicro1381 (2006).
- 776 47 Bailey, J. *et al.* Essential gene deletions producing gigantic bacteria. *PLoS*
777 *genetics* **15**, e1008195, doi:10.1371/journal.pgen.1008195 (2019).
- 778 48 Cass, J. A., Stylianidou, S., Kuwada, N. J., Traxler, B. & Wiggins, P. A. Probing
779 bacterial cell biology using image cytometry. *Molecular microbiology* **103**, 818–
780 828, doi:10.1111/mmi.13591 (2017).
- 781 49 Meberg, B. M., Sailer, F. C., Nelson, D. E. & Young, K. D. Reconstruction of
782 *Escherichia coli* mrcA (PBP 1a) mutants lacking multiple combinations of
783 penicillin binding proteins. *J Bacteriol* **183**, 6148-6149,
784 doi:10.1128/JB.183.20.6148-6149.2001 (2001).
- 785 50 Lowenthal, A. C. *et al.* Functional analysis of the *Helicobacter pylori* flagellar
786 switch proteins. *J Bacteriol* **191**, 7147-7156, doi:10.1128/JB.00749-09 (2009).
- 787 51 Taylor, J. A. *et al.* Distinct cytoskeletal proteins define zones of enhanced cell
788 wall synthesis in *Helicobacter pylori*. *Elife* **9**, doi:10.7554/eLife.52482 (2020).

- 789 52 Evinger, M. & Agabian, N. Envelope-associated nucleoid from *Caulobacter*
790 *crescentus* stalked and swarmer cells. *J Bacteriol* **132**, 294-301,
791 doi:10.1128/jb.132.1.294-301.1977 (1977).
- 792 53 Caccamo, P. D., Jacq, M., VanNieuwenhze, M. S. & Brun, Y. V. A Division of
793 Labor in the Recruitment and Topological Organization of a Bacterial
794 Morphogenic Complex. *Curr Biol* **30**, 3908-3922 e3904,
795 doi:10.1016/j.cub.2020.07.063 (2020).
- 796 54 Robertson, N., Sanders, D. P., Seymour, P. & Thomas, R. A new proof of the
797 four-colour theorem. *Electron. Res. Announc. Amer. Math. Soc.* ,
798 doi:<https://doi.org/10.1090/S1079-6762-96-00003-0> (1996).
- 799 55 Stylianidou, S., Brennan, C., Nissen, S. B., Kuwada, N. J. & Wiggins, P. A.
800 SuperSegger: robust image segmentation, analysis and lineage tracking of
801 bacterial cells. *Molecular microbiology* **102**, 690–700, doi:10.1111/mmi.13486
802 (2016).
- 803 56 Hartmann, R., van Teeseling, M. C. F., Thanbichler, M. & Drescher, K. BacStalk:
804 A comprehensive and interactive image analysis software tool for bacterial cell
805 biology. *Molecular microbiology* **114**, 140-150, doi:10.1111/mmi.14501 (2020).
- 806 57 Goni-Moreno, A., Kim, J. & de Lorenzo, V. CellShape: A user-friendly image
807 analysis tool for quantitative visualization of bacterial cell factories inside.
808 *Biotechnol J* **12**, doi:10.1002/biot.201600323 (2017).
- 809 58 Young, J. W. *et al.* Measuring single-cell gene expression dynamics in bacteria
810 using fluorescence time-lapse microscopy. *Nature protocols* **7**, 80-88,
811 doi:10.1038/nprot.2011.432 (2011).
- 812 59 O'Connor, O. M., Alnahhas, R. N., Lugagne, J. B. & Dunlop, M. J. DeLTA 2.0:
813 A deep learning pipeline for quantifying single-cell spatial and temporal
814 dynamics. *bioRxiv*, doi:<https://doi.org/10.1101/2021.08.10.455795> (2021).
- 815 60 Srivastava, N., Hinton, G., Krizhevsky, A., Sutskever, I. & Salakhutdinov, R.
816 Dropout: a simple way to prevent neural networks from overfitting. *The Journal*
817 *of Machine Learning Research* **15**, 1929-1958 (2014).
- 818 61 Kaur, H., Pannu, H. S. & Malhi, A. K. A Systematic Review on Imbalanced Data
819 Challenges in Machine Learning: Applications and Solutions. *ACM Computing*
820 *Surveys* **52**, 1-36, doi:<https://doi.org/10.1145/3343440> (2019).
- 821 62 Meberg, B. M., Sailer, F. C., Nelson, D. E. & Young, K. D. Reconstruction of
822 *Escherichia coli* mrcA (PBP 1a) mutants lacking multiple combinations of
823 penicillin binding proteins. *J Bacteriol* **183**, 6148–6149,
824 doi:10.1128/JB.183.20.6148-6149.2001 (2001).

- 825 63 Barbe, V. *et al.* Unique features revealed by the genome sequence of
826 *Acinetobacter* sp. ADP1, a versatile and naturally transformation competent
827 bacterium. *Nucleic Acids Res* **32**, 5766-5779, doi:10.1093/nar/gkh910 (2004).
- 828 64 Yu, Y. *et al.* Genomic patterns of pathogen evolution revealed by comparison of
829 *Burkholderia pseudomallei*, the causative agent of melioidosis, to avirulent
830 *Burkholderia thailandensis*. *BMC microbiology* **6**, 46 (2006).
- 831 65 Allue-Guardia, A., Echazarreta, M., Koenig, S. S. K., Klose, K. E. & Eppinger,
832 M. Closed Genome Sequence of *Vibrio cholerae* O1 El Tor Inaba Strain A1552.
833 *Genome Announc* **6**, doi:10.1128/genomeA.00098-18 (2018).
- 834 66 Stover, C. K. *et al.* Complete genome sequence of *Pseudomonas aeruginosa*
835 PA01, an opportunistic pathogen. *Nature* **406**, 959–964 (2000).

836

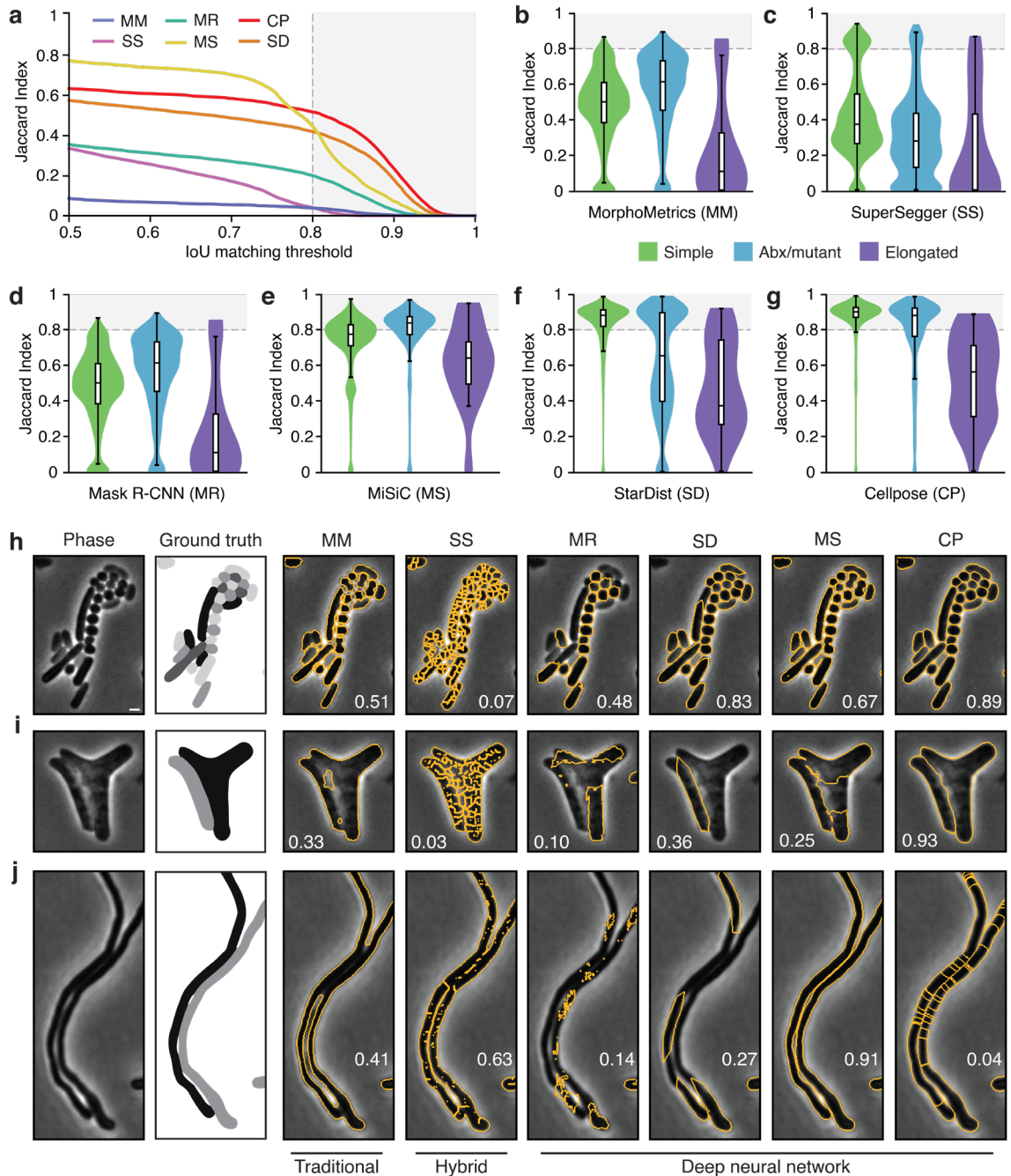


Fig. 1 | Quantitative comparison of segmentation methods distinguishes Cellpose as a high performing algorithm. (a-g) Comparison of segmentation algorithm performance on our test dataset. (a) Overall performance measured by Jaccard Index (JI). The JI was calculated at the image level and values averaged across the dataset are displayed. Algorithm abbreviations defined in B-G. (b-g) Algorithm performance partitioned by cell type (Simple, n=12,869; Abx/mutant, n=6,138; Elongated, n=46). Images were sorted into types as defined in Supplemental Table 1 (Abx, antibiotic). (h-j) Representative micrographs of cell type partitions analyzed in B-G, indicated by vertical bars at right. Ground-truth masks and predicted mask outlines generated by the indicated algorithm are displayed. Mean matched IoU values for cells shown are displayed within each micrograph. Bacteria displayed are (H) *Vibrio cholerae*, *Pseudomonas aeruginosa*, *Bacillus subtilis*, *Staphylococcus aureus*, (I) aztreonam-treated *Escherichia coli* CS703-1, and (J) *Streptomyces pristinaespiralis*. All images scaled equivalently; scale bar is 1mm.

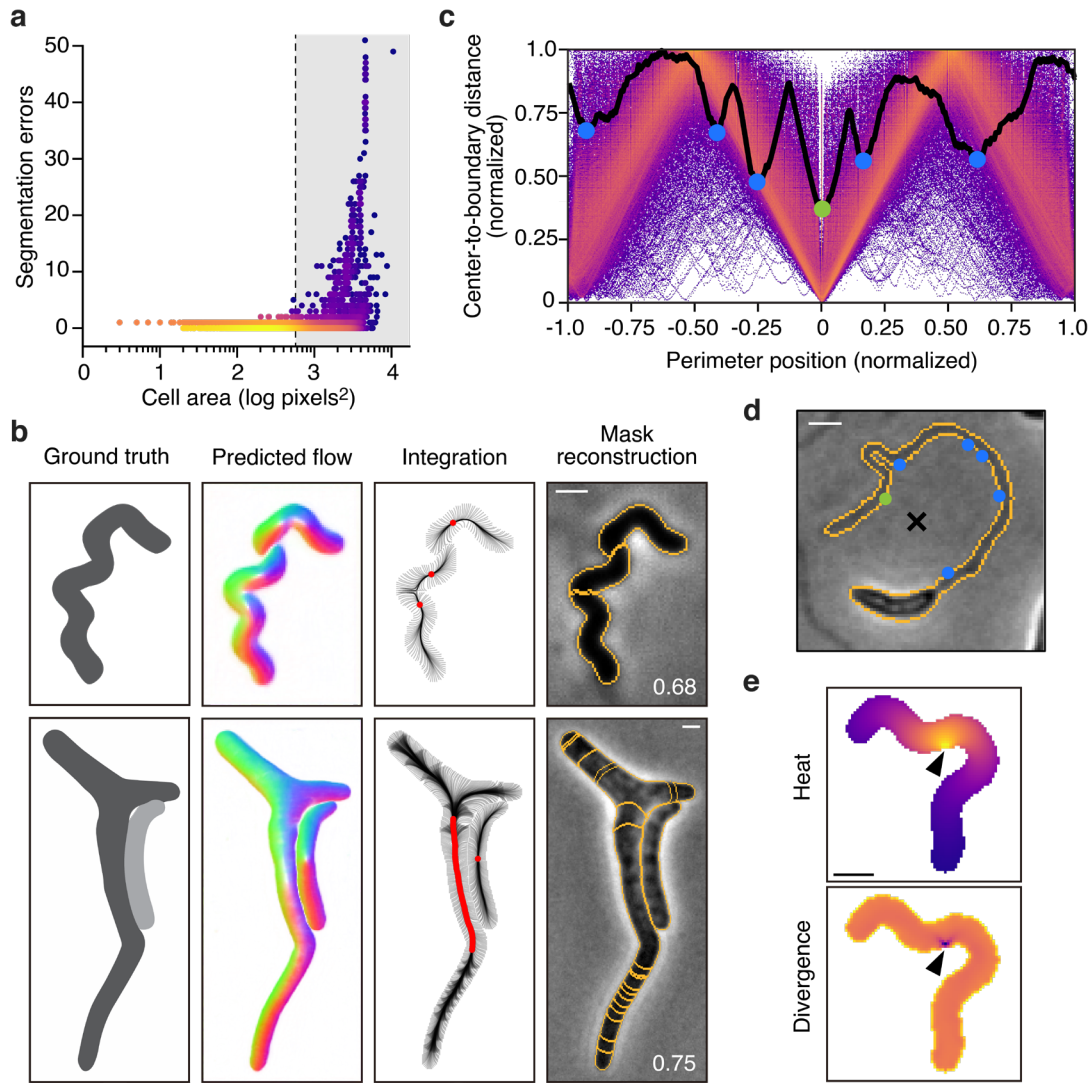


Fig. 2 | Cellpose over-segments extended, anisotropic cells. (a) Single-cell analysis of segmentation error as a function of cell area. Color represents density on a log scale. Gray box represents the top quartile of cell areas. (b) Representative examples exhibiting problematic flow fields. Corresponding boundary pixel trajectories are shown in black and final pixel locations in red. Predicted mask overlays are shown with mean matched IoU values. (c) Analysis of stochastic center-to-boundary distances. Distance from the center (median pixel coordinate) to each boundary pixel is normalized to a maximum of 1. Position along the boundary is normalized from -1 to 1 and centered on the point closest to the median pixel. Center-to-boundary for the cell in panel D is highlighted in black. (d) Representative cell with median coordinate outside the cell body (black X). Cellpose projects this point to the global minima of this function (green dot), but several other local minima exist (blue dots). (e) The heat distribution resulting from a projected cell center (black arrow). The normalized gradient corresponds to the divergence shown. Bacteria displayed are (a,e) *Helicobacter pylori*, (b) *Escherichia coli* CS703-1, both treated with aztreonam, and (d) *Caulobacter crescentus* grown in HIGG media. Scale bars are 1 μm .

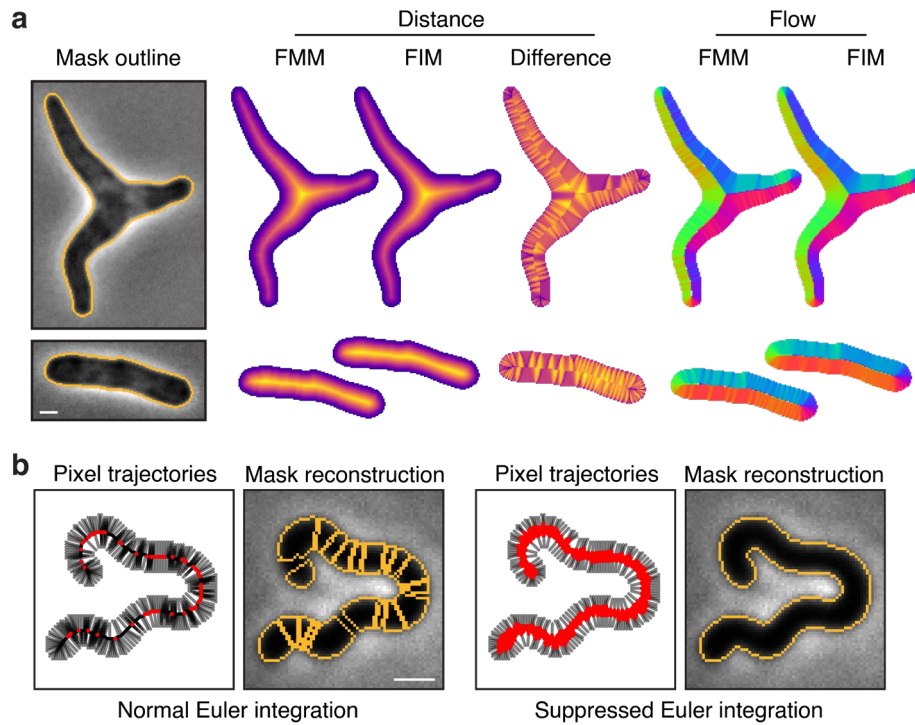


Fig. 3 | Core innovations of Omnipose. (a) Comparison of distance field algorithms and corresponding flow fields. Fast Marching Method (FMM) produces ridges in the distance field resulting from pixelation on the cell mask boundary. Our smooth FIM algorithm minimizes these features. The difference image (FIM – FMM) highlights artifacts in the FMM method. Flow fields are calculated as the normalized gradient of the distance field. Boundary pixelation affects the FMM flow field deep into the cell, regardless of cell size. (b) Comparison of mask reconstruction algorithms on a smooth flow field (not shown). Left: boundary pixel trajectories and resulting mask outlines from standard Euler integration. Right: Trajectories and mask outlines under suppressed Euler integration. Red dots indicate the final positions of all cell pixels, not only the boundary pixels for which trajectories are displayed. Bacteria displayed are (a) *Escherichia coli* CS703-1 and (b) and *Helicobacter pylori*, both treated with aztreonam. Scale bars are 1 μm .

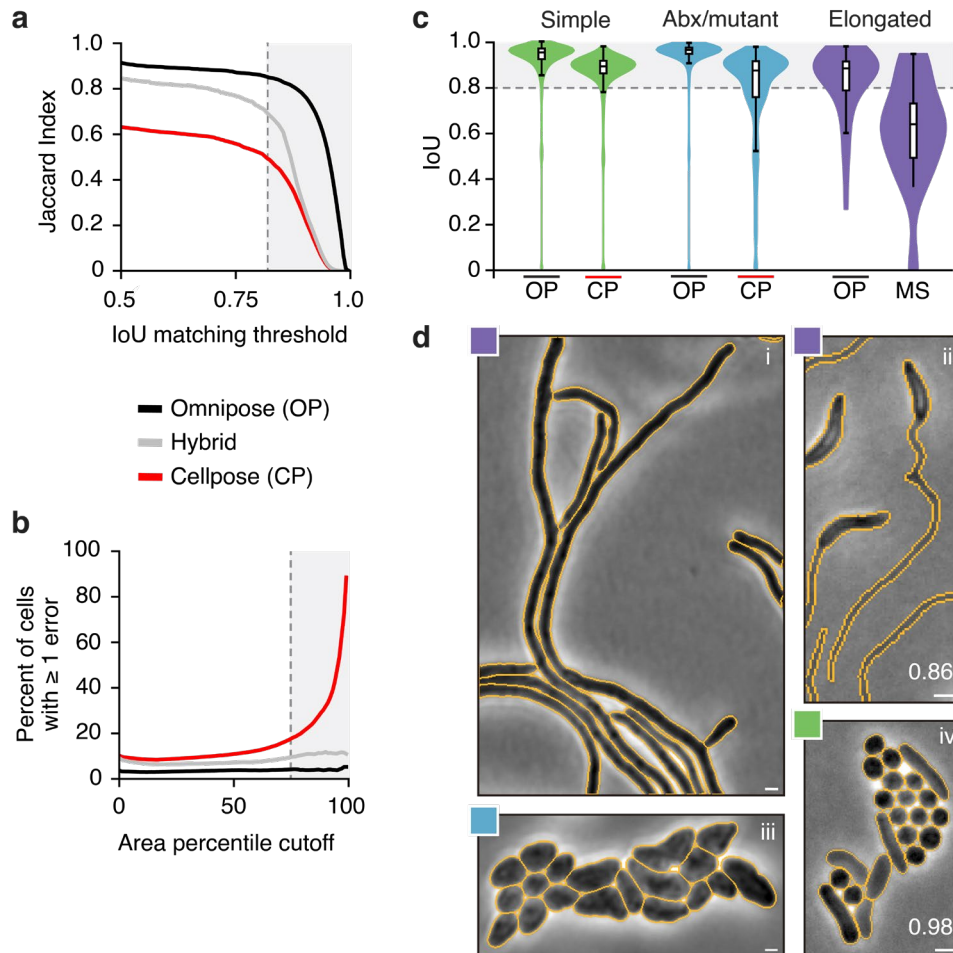


Fig. 4 | Omnipose outperforms Cellpose. (a) Overall performance measured by Jaccard Index (JI). The hybrid method (gray) is a variant of Cellpose that uses the original center-seeking flow output and the mask reconstruction of Omnipose. Gray box represents $\text{IoU} \geq 0.8$. (b) Quantification of segmentation performance by cell size. The percent of cells with at least one segmentation error is computed for cells in each area percentile group from 1 to 100. Gray box represents the top quartile. (c) Omnipose IoU distribution on our dataset compared to the next highest performing algorithm in each of three cell categories. (d) Example micrographs and Omnipose segmentation. Mean matched IoU values shown. Bacteria displayed are (i) *Streptomyces pristinaespiralis*, (ii) *Caulobacter crescentus* grown in HIGG media, (iii) *Shigella flexneri* treated with A22, (iv) mix of *Pseudomonas aeruginosa*, *Staphylococcus aureus*, *Vibrio cholerae*, and *Bacillus subtilis*. Scale bars are 1 μm .

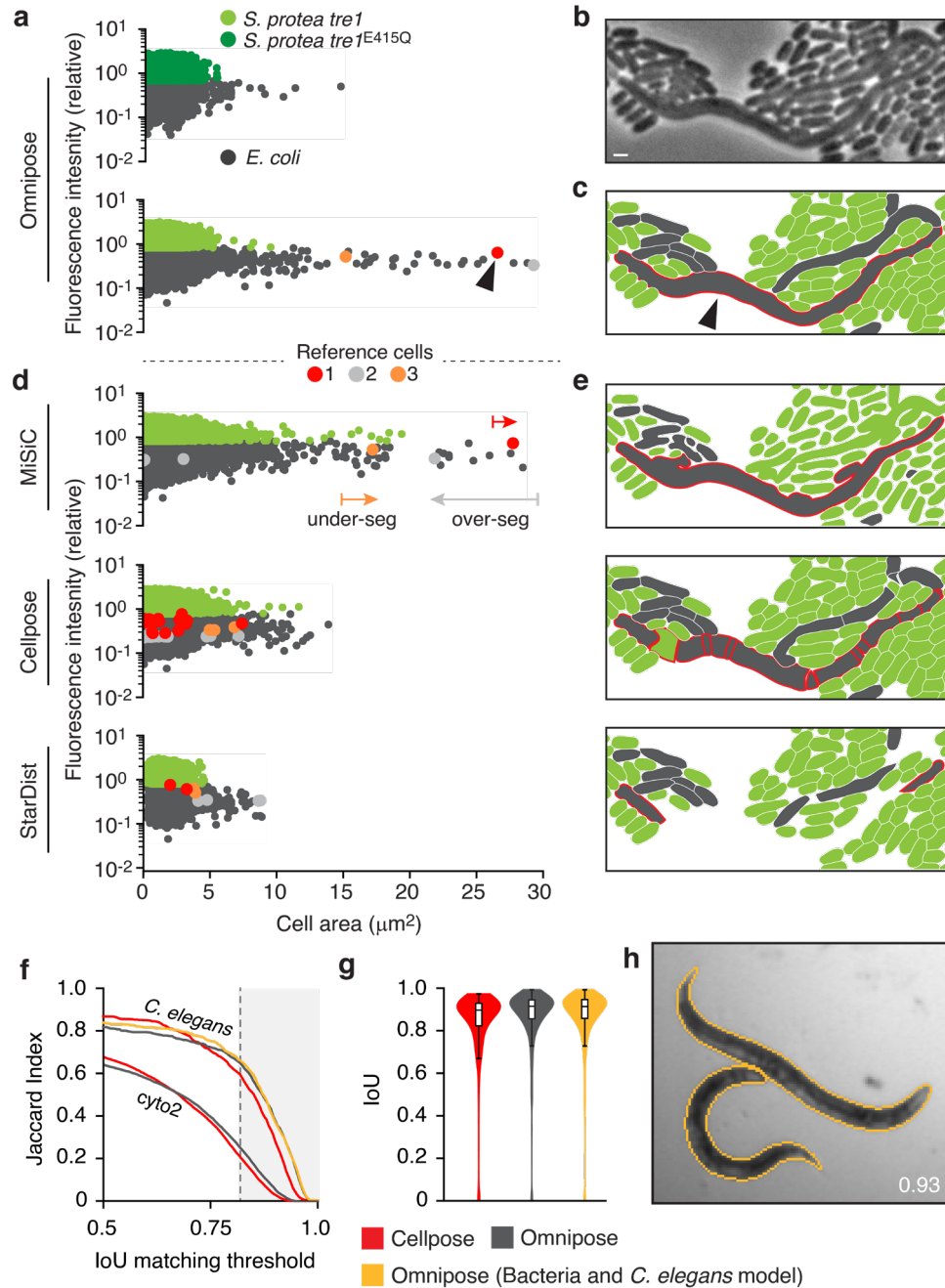
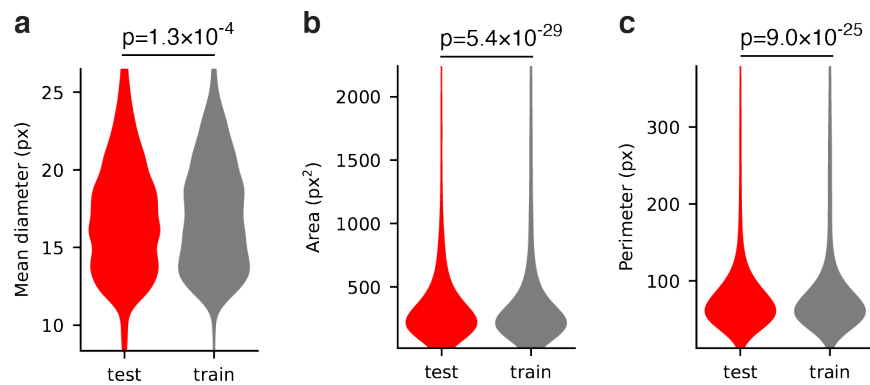
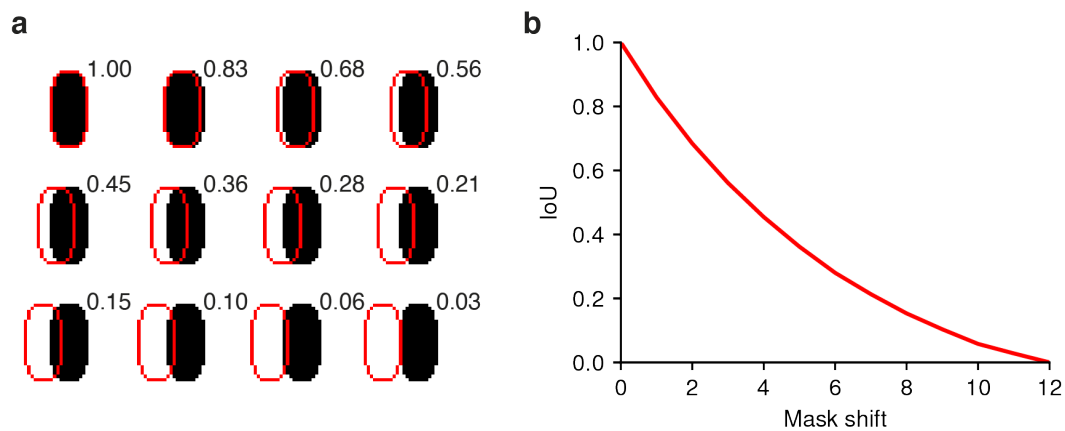


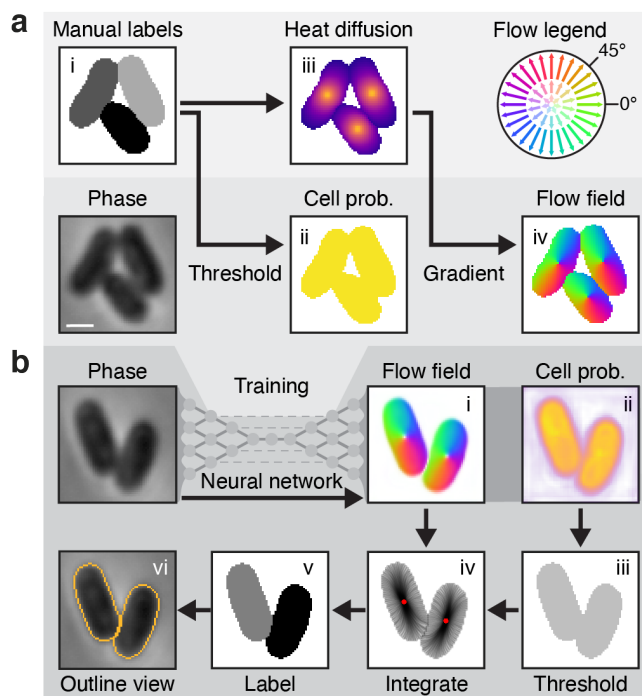
Fig. 5 | Omnipose can be applied to the study of bacterial and non-bacterial systems. (a) Fluorescence/area population profile according to Omnipose segmentation in control and experimental conditions. K-means clustering on GFP fluorescence distinguishes *S. proteamaculans tre1/tre1^{E415Q}* (light/dark green markers) from *E. coli* (gray markers). **(b)** Example of extreme filamentation of *E. coli* in response to active Tre1. **(c)** Omnipose accurately segments all cells in the image. Largest cell indicated with black arrow. **(d)** MiSiC predicts large cell masks over both species. Cellpose and StarDist fail to predict any cells above $15\mu\text{m}^2$. **(e)** Example segmentation results highlighting typical errors encountered with MiSiC (under-segmentation), Cellpose (over-segmentation), and StarDist (incomplete masks). Mask mergers cause some *E. coli* to be misclassified as *S. proteamaculans*. Scale bar is $1\mu\text{m}$. **(f)** Performance of Omnipose and Cellpose on cyto2 and *C. elegans* datasets. Results for Omnipose trained on *C. elegans* (grey) or *C. elegans* and bacterial data (yellow) are shown. **(g)** IoU distribution for the masks predicted by each method on our *C. elegans* dataset. **(h)** Example segmentation of *C. elegans* in the BBBC010 dataset.



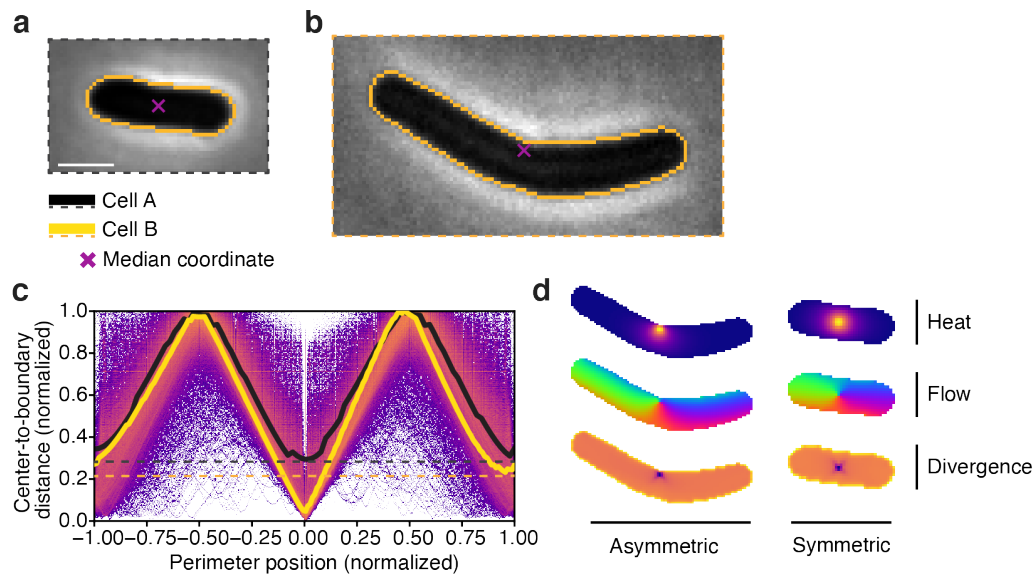
Extended Data Fig. 1 | Test dataset is representative of the training dataset. (a) Mean diameter, defined in Methods. **(b)** Cell area. **(c)** Cell perimeter. P-values are displayed for the two-sided KS test.



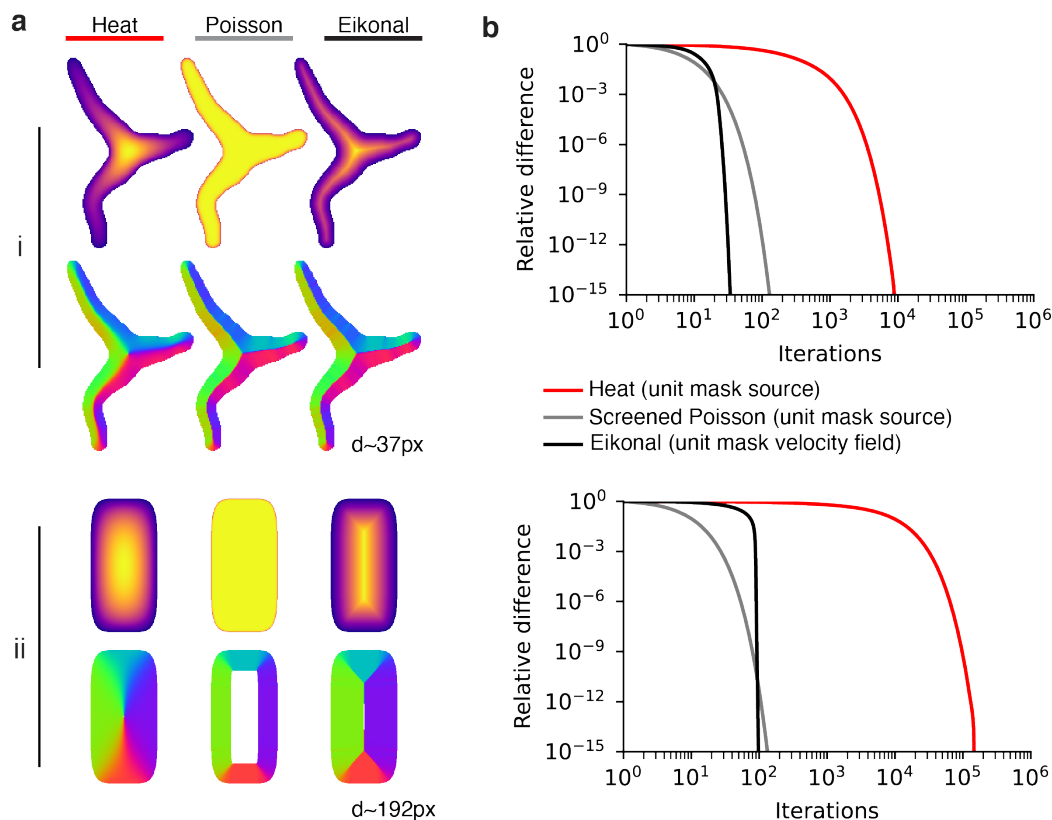
Extended Data Fig. 2 | IoU values for synthetic cell of typical size/resolution. (a) 0-12 pixel displacement of cell mask (red outline) and corresponding IoU values. **(b)** IoU decreases non-linearly for curved regions such as this synthetic cell.



Extended Data Fig. 3 | Details of the Cellpose algorithm. (a) Stages of the Cellpose training pipeline. Ground truth masks (*i*) are converted to cell probability (*ii*) by binary thresholding and a heat distribution (*iii*) by simulated diffusion from the median pixel coordinate. The flow field (*iv*) is defined by the normalized gradient of (*iii*). Color-magnitude representations of this vector field follow the flow legend diagram. The phase, cell probability, and flow fields are used to train the network. **(b)** Stages of the cellpose prediction pipeline. Phase images are processed by the trained cellpose network into the intermediate flow field and cell probability outputs (*i-ii*). A binary threshold is applied to the probability to identify cell pixels (*iii*). Pixels are Euler-integrated under the flow field until they converge at common points. Boundary pixel trajectories are depicted in *iv*. Each pixel is assigned a unique label corresponding to the center to which it converged (*v*). This segmentation result is commonly depicted in an outline view (*vi*). Bacteria shown are *Escherichia coli*. Scale bar is 1 μm .



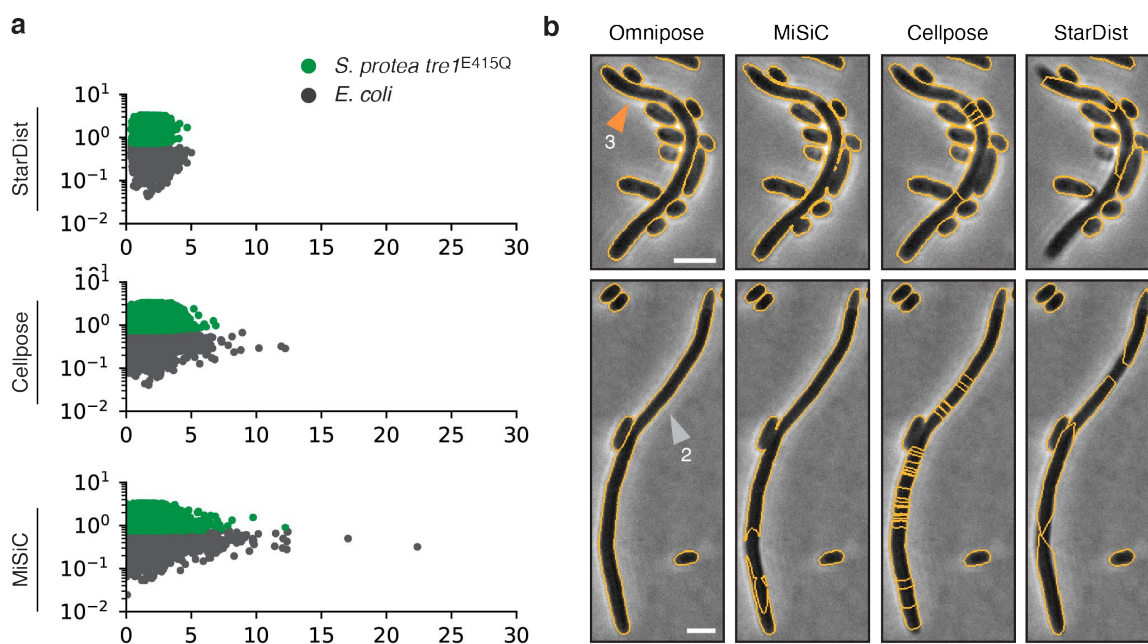
Extended Data Fig. 4 | Median coordinates are asymmetrically localized. (a) Center-to-boundary distance highlighted for two cells with non-projected median coordinates. Dashed lines indicate the larger of the two minima along the medial axis. (b) Rod-shaped *E. coli* with symmetric median coordinate. Symmetry of the center is reflected in A by equal high and low points corresponding to the extremal points along the long and short axes of the cell. (c) Curved *B. subtilis* with median coordinate asymmetrically close to the cell boundary. This asymmetry is reflected in A by a secondary minimum above the global minimum corresponding to the diametrically opposing point along the short axis of the cell. (d) These centers result in distinct flow fields reflecting the (a)symmetric of the cell center. Bacteria shown are (a) *Escherichia coli* and (b) *Bacillus subtilis*. Scale bar is 1 μm . Images scaled equivalently.



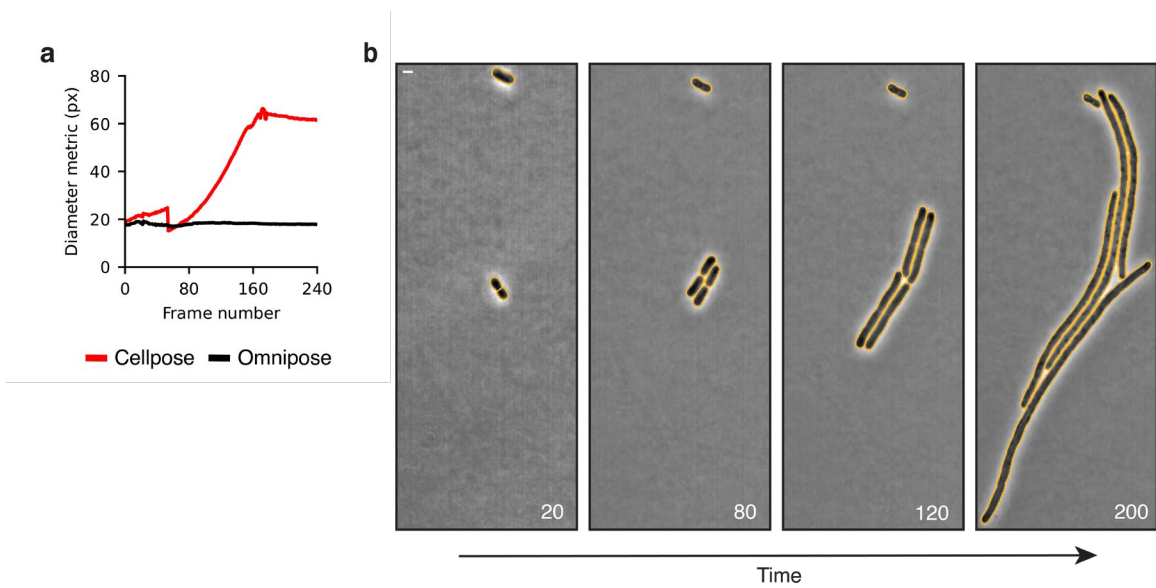
Extended Data Fig. 5 | Comparison of three algorithms for computing center-independent flow fields.

Each field is defined by a partial differential equation with the mask at the source: time-independent heat equation, the screened Poisson equation, and the Eikonal equation. We solve these equations with iterative relaxation (see Methods). (a) Two example cells, the first drawn from our dataset with a mean diameter of 37px and a synthetic rod-shaped cell with a mean diameter of 192px. Cell (i) exhibits heat-derived flow components pointing toward the skeleton near boundaries and toward the global cell center at the skeleton. Center-seeking flow components become problematic for mask reconstruction for more complicated cell geometries, namely those with oscillating thickness. The screened Poisson and Eikonal equations produce nearly identical flow fields (same direction, normalized magnitude). Cell (ii) reveals a core flaw in the screened Poisson solution: its derivative exceeds our available numerical precision, leading to a vanishing flow field at the center where the solution plateaus. Any cells of this size or larger will exhibit this issue.

(b) Convergence measured by the average difference at each iteration (maximum normalized to 1) for cells (i, ii). Our Eikonal solution converges faster than the other methods by a wide margin at typical cell diameters (i).



Extended Data Fig. 6 | Controls and additional examples. (a) Controls segmented by StarDist, Cellpose, and MiSiC. Notably, Cellpose and MiSiC exhibit an enrichment of larger cells even in the control, a consequence of both under-segmented (merged) cells as well as fragments of over-segmented large cells. **(b)** Cells 2 and 3 highlighted in orange and gray plotted in Fig. 5a,d. Scale bars are 1 μm .



Extended Data Fig. 7 | Comparison of diameter metrics on a filamentous microcolony time lapse. (a). Cellpose diameter metric is the diameter of the circle with equivalent area. Omnipose diameter metric is proportional to the mean of the distance transform. **(b)** Bacteria displayed are *A. baylyi* transformed with a $\Delta ftsN::kan$ PCR fragment. Scale bar is 1 μm .

Extended Data Table 1.

Species	Strain	Image count	Cell Count	Cells in GT	Percent of GT	Notes
<i>Escherichia coli</i>	DH5 α	1378	98200	9733	20.6	Dense microcolonies grown on minimal media. Thin phenotype. ITPG-induced GFP cytosol marker. Time lapse. Imaged by the Wiggins lab.
		141	4536	4395	9.3	Dense microcolonies on LB. Time lapse. Imaged by the Wiggins lab.
		2	2277	-	-	Treatment with cephalixin. Tn7::GFP. Imaged by the Mougous lab.
	CS703-1 ⁶²	80	23169	1299	2.6	Mutant grown on LB and aztreonam. Elongated and branching phenotypes. Time lapse. Imaged by the Mougous lab.
<i>Shigella flexneri</i>	M90T	117	256618	1409	3.0	Treatment with A22. Tn7::GFP. Frames selected from time lapse after 1hr growth. Imaged by the Mougous lab.
		6	4482	4318	9.2	Treatment with cephalixin. Tn7::GFP. Frames selected from time lapse after 1hr growth. Imaged by the Mougous lab.
<i>Francisella tularensis subsp. novicida</i>	U112	5	20166	496	1.1	Small and extremely low-contrast cells. Tn7::GFP. Imaged by the Mougous lab.
<i>Acinetobacter baylyi</i>	ADP1 ⁶³	2169	60601	3336	7.1	Deletion of essential gene <i>murA</i> . Rounded phenotype. Time lapse. Imaged by the Wiggins lab.
		241	1313	1133	2.4	Deletion of essential gene <i>ftsN</i> . Filamentous phenotype. Time lapse. Imaged by the Wiggins lab.
		540	10013	2227	4.7	Deletion of essential gene <i>dnaA</i> . Filamentous phenotype. Time lapse. Imaged by the Wiggins lab.
<i>Burkholderia thailandensis</i>	E264 ⁶⁴	30	62005	5122	10.9	Selected panels from a self-intoxication experiment. Cells exhibit internal structure and low contrast in microcolonies. Tn7::GFP. Time lapse. Imaged by the Mougous lab.
<i>Helicobacter pylori</i>	LHS100 ⁵⁰	15	13014	-	-	Helical phenotype. Grown, fixed, and stained with Alexaflour 488 in the lab of

						Nina Salama. Imaged by the Mougous lab.
		19	1668	701	1.5	Treated with aztreonam. Filamentous, helical phenotype. Grown, fixed, and stained with Alexaflour 488 in the lab of Nina Salama. Imaged by the Mougous lab.
<i>Caulobacter crescentus</i>	NA1000 ⁵²	4	1787	756	1.6	Grown in HIGG media to induce stalk phenotype. Cultivation and imaging done in the lab of Yves Brun.
<i>Streptomyces pristinaespiralis</i>	NRRL 2958	17	2339	270	0.6	Grown on rich media to induce filamentous phenotype. Imaged by the Mougous lab.
<i>Vibrio cholerae</i>	A1552 ⁶⁵	2	2627	2265	4.8	Cells have short but curved morphology and form dense, low-contrast microcolonies. Tn7::GFP. Obtained from the lab of Fitnat Yildiz. Imaged in the Mougous lab.
<i>Serratia proteamaculans</i> <i>E. coli</i>	568 DH5 α	43	100146	1244	2.6	1:1 mixture. <i>S.p.</i> labelled via Tn7::GFP, <i>E.c.</i> unlabeled. Time lapse. Imaged in the Mougous lab.
<i>Pseudomonas aeruginosa</i> <i>Staphylococcus aureus</i>	PAO1 ⁶⁶ USA300	3	2662	3688	7.8	1:1 mixture. <i>P.a.</i> labelled via Tn7::GFP, <i>S.a.</i> unlabeled. Imaged in the Mougous lab.
<i>P. aeruginosa</i> <i>S. aureus</i> <i>V. cholerae</i> <i>Bacillus subtilis</i>	PAO1 USA300 A1552 HM1350	21	33281	4678	9.9	1:1:1:1 mixture. <i>P.a.</i> and <i>V.c.</i> labelled via Tn7::GFP, <i>S.a.</i> and <i>B.s.</i> labelled with red membrane dye. Imaged in the Mougous lab.
		4833	700904	47070	100	